

Half-Megasecond *Chandra* Spectral Imaging of the Hot Circumgalactic Nebula around Quasar Mrk 231

S. Veilleux^{1,2}, S. H. Teng³, D. S. N. Rupke⁴, R. Maiolino^{5,6}, & E. Sturm⁷

ABSTRACT

A deep 400-ksec ACIS-S observation of the nearest quasar known, Mrk 231, is combined with archival 120-ksec data obtained with the same instrument and setup to carry out the first ever spatially resolved spectral analysis of a hot X-ray emitting circumgalactic nebula around a quasar. The $\sim 65 \times 50$ kpc X-ray nebula shares no resemblance with the tidal debris seen at optical wavelengths. One notable exception is the small tidal arc ~ 3.5 kpc south of the nucleus where excess soft X-ray continuum emission and Si XIII 1.8 keV line emission are detected, consistent with star formation and its associated α -element enhancement, respectively. An X-ray shadow is also detected at the location of the 15-kpc northern tidal tail, implying a foreground hydrogen column density of at least 2.5×10^{21} cm⁻². The hard X-ray continuum emission within ~ 6 kpc of the center is consistent with being due entirely to the bright central AGN and the wings of the *Chandra* point spread function. The soft X-ray spectrum of the outer (>6 kpc) portion of the nebula is best described as the sum of two thermal components of temperatures ~ 3 and ~ 8 million K with spatially uniform super-solar α element abundances, relative to iron. This result implies enhanced star formation activity over $\sim 10^8$ yrs accompanied with redistribution of the metals on large scale. The low-temperature thermal component is not present within 6 kpc of the nucleus, suggesting extra heating in this region from the circumnuclear starburst, the central quasar, or the wide-angle quasar-driven outflow identified from optical IFU

¹Department of Astronomy, University of Maryland, College Park, MD 20742, USA; veilleux@astro.umd.edu

²Joint Space-Science Institute, University of Maryland, College Park, MD 20742, USA

³Observational Cosmology Laboratory, NASA Goddard Space Flight Center, Greenbelt, MD 20771, USA

⁴Department of Physics, Rhodes College, Memphis, TN 38112, USA

⁵Cavendish Laboratory, University of Cambridge, 19 J.J. Thomson Ave., Cambridge, CB3 0HE, UK

⁶Kavli Institute for Cosmology, Madingley Road, Cambridge, CB3 0HA, UK

⁷Max-Planck-Institut für extraterrestrische Physik, Postfach 1312, D-85741 Garching, Germany

spectroscopy on a scale of $\gtrsim 3$ kpc. Significant azimuthal variations in the soft X-ray intensity are detected in the inner region where the outflow is present. The soft X-ray emission is weaker in the western quadrant, coincident with a deficit of H α emission and some of the largest columns of neutral gas outflowing from the nucleus. Shocks created by the interaction of the wind with the ambient ISM may heat the gas to high temperatures at this location. The tentative detection at the ~ 2 -sigma level of He-like Fe XXV 6.7 keV line emission extending ~ 3 kpc north-west of the nucleus provides some support to this scenario, if it is produced by ~ 70 million K gas rather than high-mass X-ray binaries.

Subject headings: galaxies: active — galaxies: starburst — ISM: jets and outflows — quasars: individual (Mrk 231) — X-rays: galaxies

1. Introduction

In the past few years, Mrk 231 has become arguably the best laboratory to study quasar feedback in action. One reason for this is the proximity of Mrk 231: at a distance¹ of only 178 Mpc, it is the nearest quasar known (Boksenberg et al. 1977) and thus provides an excellent linear resolution ($1'' = 0.863$ kpc). But there are several other reasons why Mrk 231 has attracted attention. It is one of the best local examples of powerful quasar and starburst activity triggered by a recent merger (e.g., Hamilton & Keel 1987; Hutchings & Neff 1987; Surace et al. 1998; Veilleux et al. 2002, 2006). It is a morphologically disturbed ultraluminous infrared galaxy (ULIRG) with an infrared ($8 - 1000 \mu\text{m}$) luminosity $\log[L_{\text{IR}}/L_{\odot}] = 12.54$ and a bolometric luminosity² $\log[L_{\text{BOL}}/L_{\odot}] \approx 12.60$ that is produced at $\sim 70\%$ by the quasar and $\sim 30\%$ by a starburst with a star formation rate $\text{SFR} \sim 140 M_{\odot} \text{ yr}^{-1}$ (Veilleux et al. 2009). More relevant to the issue of feedback, Mrk 231 is also a member of the rare class of iron low-ionization broad absorption-line (FeLoBAL) quasars, with an unresolved nuclear outflow with a velocity of up to $\sim -8000 \text{ km s}^{-1}$ measured in Na I D 5890, 5896 Å and several other optical and ultraviolet lines (Boksenberg et al. 1977; Rudy, Foltz, & Stocke 1985; Hutchings & Ne 1987; Boroson et al. 1991; Kollatschny, Dietrich, & Hagen 1992; Forster, Rich, & McCarthy 1995; Smith et al. 1995; Rupke, Veilleux, & Sanders 2002; Gallagher et al. 2002, 2005; Veilleux et al. 2013a). Finally, and most relevant to the

¹Based on a redshift $z = 0.0422$ and a cosmology with $H_0 = 73 \text{ km s}^{-1} \text{ Mpc}^{-1}$, $\Omega_{\text{matter}} = 0.27$, and $\Omega_{\text{vacuum}} = 0.73$.

²This estimate for the bolometric luminosity includes all IR and non-IR contributions and is derived by simply assuming $L_{\text{BOL}} = 1.15 L_{\text{IR}}$, typical for ULIRGs (e.g., Sanders & Mirabel 1996).

present paper, recent observations have revealed that Mrk 231 also hosts a powerful spatially resolved optically-detected wind with velocities in excess of $\sim -1000 \text{ km s}^{-1}$ (Rupke, Veilleux, & Sanders 2005c; Rupke & Veilleux 2011, 2013, hereafter RV11 and RV13, respectively).

The optical observations of RV11 and RV13 show that this wind is predominantly neutral (traced in absorption by Na I D) and extends out to at least $\sim 3 \text{ kpc}$. The neutral wind gas is symmetrically distributed around the nucleus and presents a uniform velocity field with no obvious spatial gradient. These results indicate the presence of a wide-angle outflow that is expelling gas at a rate of at least $\sim 200 M_{\odot} \text{ yr}^{-1}$ out of the nuclear region (RV13). The axis of this conical outflow is roughly along the minor axis of the near face-on sub-kpc molecular / stellar disk (e.g., Downes & Solomon 1998; Davies et al. 2004). Remarkably, a number of recent far-infrared and mm-wave studies (Fischer et al. 2010; Feruglio et al. 2010; Sturm et al. 2011; Aalto et al. 2012; Cicone et al. 2012; Gonzalez-Alfonso et al. 2014) have inferred that a similar (if not larger) amount of molecular gas is entrained in this outflow, reaching velocities that are similar to those measured optically in the spatially resolved neutral wind. This multi-phase wind is thus potentially a life-changing event for Mrk 231, capable of displacing most of the neutral and molecular gas from the nucleus, and thus quenching nuclear star formation and also possibly the quasar activity, on a timescale of only a few $\times 10^6 \text{ yr}$. This is the essence of quasar feedback, which is purported to transform many gas-rich mergers into inactive bright elliptical galaxies (di Matteo, Springel, & Hernquist 2005; Murray, Quataert, & Thompson 2005; Veilleux, Cecil, & Bland-Hawthorn 2005; Veilleux et al. 2013b; Cicone et al. 2014).

Not surprisingly, Mrk 231 has been the subject of numerous X-ray studies, using the whole gamut of high-energy space facilities, starting with *Einstein*, *ROSAT*, *ASCA*, and *CGRO* (e.g., Eales & Arnaud 1988; Dermer et al. 1997; Turner 1999; Maloney & Reynolds 2000). It was observed with *Chandra* on multiple occasions: once in 2000 ($\sim 40 \text{ ksec}$; Gallagher et al. 2002), three times in 2003 ($\sim 40 \text{ ksec}$ each spanning over three weeks; Gallagher et al. 2005), and once again in 2010 ($\sim 5\text{-ksec}$ snapshot; PI Garmire). The 2000-2003 data were independently re-analyzed by Ptak et al. (2003), Grimes et al. (2005), and Teng & Veilleux (2010). Mrk 231 was observed with *XMM-Newton* in 2001 ($\sim 20 \text{ ksec}$; Turner & Kraemer 2003) and at 12 – 60 keV with *BeppoSAX* at the end of 2001 (Braitto et al. 2004). The combined *XMM-Newton* + *BeppoSAX* spectrum of the nucleus suggests the existence of a highly absorbed ($N_H \sim 2 \times 10^{24} \text{ cm}^{-2}$), powerful (intrinsic 2-10 keV luminosity of $\sim 1 \times 10^{44} \text{ erg s}^{-1}$) AGN. The direct AGN continuum appears to be only detected beyond $\sim 10 \text{ keV}$, while reprocessed radiation through scattering and/or reflection dominates the observed 2-10 keV emission (Braitto et al. 2004). A more recent (April 2011) 200-ksec observation of Mrk 231 with *Suzaku* by Piconcelli et al. (2013) indicates that the absorbing material is patchy, now letting through a significantly larger fraction of the direct $< 10 \text{ keV}$ AGN contin-

uum than in 2001. This patchy material may also be responsible for the scattering/reflection itself and the optical/UV LoBAL systems (e.g., Rupke et al. 2002, 2005c; Gallagher et al. 2005; Veilleux et al. 2013a and references therein). The recent high-energy (3 – 30 keV) *NuSTAR* observation of Mrk 231, supplemented with our new and simultaneous low-energy (0.5-8 keV) data from *Chandra*, puts into question the existence of Compton-thick material in front of this source (Teng et al. 2014). Mrk 231 was detected at high energies, though at much fainter flux levels than previously reported, likely due to contamination in the large apertures of previous non-focusing hard X-ray telescopes. The full band (0.5 – 30 keV) X-ray spectrum of Mrk 231 suggests that the AGN in this object is absorbed by a patchy and Compton-thin column of $N_{\text{H, AGN}} = 1.12_{-0.24}^{+0.29} \times 10^{23} \text{ cm}^{-2}$.

A strong thermal (Mewe-Kaastra-Liedahl or MEKAL) component with $kT \sim 0.7 - 0.8$ keV is also contributing to the soft X-ray band of the nuclear spectrum (e.g., Gallagher et al. 2002, 2005; Ptak et al. 2003; Teng & Veilleux 2010; Teng et al. 2014). But this nuclear soft X-ray emission is just the tip of the iceberg: The *Chandra* ACIS-S observations by Gallagher et al. (2002, 2005) have revealed a spectacular soft X-ray nebula extending out to $\sim 30''$ (~ 25 kpc) from the nucleus of Mrk 231 (see also Grimes et al. 2005). A reanalysis of these data reveals that the morphology of the inner portion of this nebula is similar to that of the $\text{H}\alpha$ emission mapped by RV11. In particular, there appear to be soft X-ray enhancements immediately east of the nucleus and ~ 3.5 kpc south of the nucleus, respectively, coincident with an H II region and the tidal arc seen in RV11. These data show tantalizing evidence for spatial variations in the properties of the X-ray gas, but the counts are not sufficient to draw statistically significant conclusions.

The present paper describes the results from our analysis of a considerably deeper *Chandra* ACIS-S data set, combining a new 400-ksec observation with the 2003 archival data obtained with the same instrument and in the same configuration. The results from a detailed analysis of the new *Chandra* data on the central AGN, in combination with the high-energy *NuSTAR* spectrum, were presented in Teng et al. (2014). Here, we focus our attention on the extended X-ray emission of Mrk 231 and discuss whether some of this emission may relate to the spatially resolved galactic wind. The acquisition of the data is discussed in §2, followed by a description of the results from the image and spectral analyses (§3) and a discussion of the implications (§4). The conclusions are summarized in §5.

2. Observations

The rationale behind the setup used for the new 400-ksec observation (PID 13700587; PI Veilleux) was to match the observational parameters of the 3×40 -ksec exposures obtained in

2003 by Gallagher et al. (2005) and thus facilitate the task of combining both data sets into a single 0.52-Msec exposure. The other *Chandra* data sets obtained before or after 2003 are considerably shallower or acquired in a different mode so no attempt was made to combine them with the present data set. Mrk 231 was aimed at the back-illuminated S3 detector of ACIS (Garmire et al. 2003). Due to scheduling constraints, the planned 400-ksec observation was divided into three segments of 40.97, 182.02, and 177.99 ksec, obtained close in time (23, 24, and 27 August 2012, respectively) to reduce the effects of variability in the AGN and background (e.g., solar flares). All of the observations were performed in 1/2 subarray mode in order to avoid pileup and take advantage of *Chandra*'s excellent angular resolution.

3. Results

3.1. Image Analysis

The data from the 2003 and 2012 epochs were combined together. Both epochs were reduced using CIAO version 4.5 and CALDB version 4.5.6. This processing incorporates energy-dependent subpixel event repositioning (EDSER algorithm; Li et al. 2004) which delivers optimized image resolution by subpixel repositioning of individual X-ray events. These data were re-processed to verify that this optimization was indeed carried out properly and to check against flares using the *Python*-based “deflare” routine, which discards any data with count rate that is 3 standard deviations from the mean of the distribution. We make no attempt to deconvolve the data using, e.g., Lucy or EMC2 algorithms (Lucy 1974; Esch et al. 2004; Karovska et al. 2005). This strategy better preserves diffuse features and possible slight asymmetries in the point spread function (PSF).³ The image data were merged for analysis using the CIAO script “merge_obs”. All of the data were reprojected to a common reference position. This minimizes the effect of relative astrometric errors on the final merged image which might produce false morphological features. The absolute astrometric error for ACIS-S is $\sim 0''.6$. We checked our final image against the VLA FIRST position of Mrk 231. The absolute astrometric offset was measured to be $0''.09$.

The images derived from the combined data set are shown in Figure 1. The full-band (0.5 – 8 keV) images (top row in Figure 1) show a large complex of emission extending over a total scale of at least $80''$ or ~ 65 kpc in the north-south direction and $60''$ or ~ 50 kpc in the east-west direction. This emission is not distributed symmetrically with respect to the nucleus, extending further to the south (~ 40 kpc) than to the north (~ 18 kpc), and further

³CIAO version 4.5 manual: <http://cxc.harvard.edu/ciao/caveats/psf.artifact.html>.

east (~ 26 kpc) than west (~ 16 kpc). This high-S/N data set also reveals that the X-ray emission is highly clumpy or filamentary. The morphology of the large-scale X-ray emission does not share a strong resemblance with that of the tidal debris (upper middle panel of Figure 1; RV11; Koda et al. 2009). In fact, the X-ray emission on the north side is *weaker* at the position of the tidal tail.⁴ This indicates that foreground tidal material absorbs some of the X-ray photons along the line of sight. Iwasawa et al. (2011) reported a similar X-ray “shadow” of a tidal tail in the ULIRG Mrk 273. In §3.2.4, we derive a lower limit on the column density of the northern tidal tail in Mrk 231 based on the apparent deficit of X-ray emission at this location.

However, it is also clear that not all tidal features cast an X-ray shadow. The bright tidal arc located ~ 3.5 kpc south of the nucleus coincides with X-ray enhancements (upper right panel of Figure 1). This tidal feature is known to be forming stars and may even be powering its own supernova-driven outflow (RV11). The spectral properties of the X-ray emitting gas at the location of this tidal arc are discussed in §3.2.3; the results from this spectral analysis confirm the presence of star-forming complexes at this location.

The false color maps shown on the bottom row of Figure 1 indicate a trend with distance from the nucleus where the extended emission is distinctly softer than the nuclear and circumnuclear emission. This is illustrated more clearly in Figures 2 and 3, where the azimuthally-averaged radial profile and two-dimensional map of the hardness ratio [defined as $(HX - SX) / (HX + SX)$, where HX and SX are the 2 – 8 keV and 0.5 – 2 keV fluxes, respectively] are presented. Also shown in Figure 2 are the azimuthally-averaged radial profiles of the background-subtracted soft and hard X-ray emission fit with a two-component β -model:

$$\Sigma(R) = \Sigma_0 [1 + (R/R_0)^2]^{-3\beta+0.5},$$

where $\Sigma(R)$ is the azimuthally-averaged surface brightness profile, Σ_0 is the central surface brightness, R_0 is the core radius, and β is the power-law index that quantifies the slope at large radii. Note the dependence of the surface brightness profile on X-ray energies, resulting in variations of the hardness ratio. While the hardness ratio profile within ~ 2 kpc is somewhat affected by the energy dependence of the central PSF associated with the AGN (the PSF is broader at higher energies; Wang et al. 2014), the small values of the hardness ratios at $R \gtrsim 2$ kpc, where the flux contribution from the central PSF is considerably smaller, reflect the softness of the extended nebula. The right panel in Figure 3 also suggests the presence of a slight asymmetry in the hardness ratio map of the central region ($R \lesssim 2$ kpc),

⁴The X-ray emission at the position of the tidal tail that extends more than 30 kpc south of the nucleus (Koda et al. 2009) also seems weaker, but the effect is less significant (see top middle panel of Figure 1).

with higher hardness ratios measured west of the nucleus. This result will be revisited in §3.2, taking into account the spectral responses of *Chandra* at various epochs.

3.2. Spectral Analysis

For each observation, individual spectra were extracted from pre-determined extraction regions (see Figure 4) and then combined together into a merged spectrum for each region using the “combine” keyword in the *specextract* function in CIAO 4.5. All spectra used the same background extraction region to assure that differences are not due to changes in the background since we expect the variability in the background to be small from observation to observation. All spectra were binned to at least 15 counts per bin, unless noted otherwise (e.g., when the counts were high, we binned by S/N). XSPEC version 12.8.0k was used for this analysis. The errors quoted below are at the 90% confidence level.

The different regions were modeled *simultaneously* using a procedure that is similar to that used to fit the quasars in Teng & Veilleux (2010). We initially started with the nuclear portion of the *NuSTAR* model (hereafter called the nuclear *NuSTAR* model) i.e., the model that was found by Teng et al. (2014) to best fit the combined *NuSTAR* + *Chandra* nuclear data. In this model, the direct AGN emission is absorbed and scattered by a patchy torus with $N_{\text{H, AGN}} = 1.12^{+0.29}_{-0.24} \times 10^{23} \text{ cm}^{-2}$. More specifically, the best-fit model includes a leaky MYTorus component for the AGN emission (Murphy & Yaqoob 2009), an Fe line at 6.7 keV from He-like Fe XXV, and a heavily obscured ($N_{\text{H, nuclear HMXB}} = 2.4 \times 10^{23} \text{ cm}^{-2}$) component from high-mass X-ray binaries (HMXBs) associated with the nuclear star formation (SFR of $\sim 140 M_{\odot} \text{ yr}^{-1}$). The *NuSTAR* model of Teng et al. (2014; see Table 1 in that paper for an equation form of the best-fit *NuSTAR* model) also includes a two-component MEKAL (Mewe-Kaastra-Liedahl) model of the emission from the hot diffuse gas within the NuSTAR aperture (recall that the half-power diameter of NuSTAR is $\sim 58''$). Since our *Chandra* observations resolve this diffuse emission, these MEKAL components are treated separately from the nuclear component in the present paper (their intensities and temperatures are allowed to vary independently of the nuclear *NuSTAR* model; see below).

The flux of the nuclear *NuSTAR* model was allowed to vary with position in the nebula, but the relative intensities of the various components of this model were held fixed. Previous studies (e.g., Gallagher et al. 2002; Teng et al. 2014) have shown that the hot diffuse gas is best described as the sum of up to two thermal (MEKAL) plasma components. For completeness, we also explore in this paper the possibility that the hot diffuse gas is shocked plasma. We confirm that the best-fit models of our deeper *Chandra* data requires at least one MEKAL component or one shock component to explain the soft X-ray emission. In all

fits, we chose to tie the temperature(s) of the MEKAL or shock component(s) to be the same in all regions and look for spatial variations in its (their) intensity (intensities). At a few locations in the nebula, excess hard X-ray emission was detected and attributed to HMXBs from circumnuclear star-forming regions. This contribution was modeled as a cutoff power-law model with cutoff energy of 10 keV and a fixed Γ of 1.1, following Braito et al. (2004). We assumed no intrinsic absorption to the nebula, i.e., the hydrogen column density outside of the nucleus was fixed to the Galactic value. Finally, lines were identified using the ATOMDB database (atomdb.org). Line identification was carried out by choosing the line in the energy range with the expected highest relative intensity.

In summary, the best-fit model can be described in equation form as:

$$\begin{aligned} \text{Model} = & N_{\text{H, Galactic}} \times \{f_{\text{nuclear NuSTAR}} \times N_{\text{H, nucleus}} \times (\text{MYTorus}[N_{\text{H, AGN}}, PL_{\text{AGN}}] \\ & + f_{\text{C-thin}} \times PL_{\text{AGN}} + N_{\text{H, nuclear HMXB}} \times PL_{\text{nuclear HMXB}}^{\text{cutoff}}) \\ & + (N_{\text{H, host HMXB}} \times PL_{\text{host HMXB}}^{\text{cutoff}} + \text{line}[1 - 4] + \text{Nebula})\}, \end{aligned}$$

where $N_{\text{H, Galactic}} = 1.26 \times 10^{20} \text{ cm}^{-2}$, the Galactic column density in the direction of Mrk 231 (Dickey & Lockman 1990), $f_{\text{nuclear NuSTAR}}$ is the fraction (< 1) of the NuSTAR spectrum of Teng et al. (2014), minus the two MEKAL models of the nuclear diffuse emission, within the given aperture, $N_{\text{H, nucleus}}$ is an additional absorbing column in the line of sight toward the nucleus, not seen in the shallower⁵ *Chandra* spectrum of Teng et al. (2014), $N_{\text{H, AGN}}$ is the absorbing column of the AGN emission calculated as part of the MYTorus model and PL_{AGN} is the direct AGN emission within the MYTorus model that also includes the scattered fraction and Fe lines, $f_{\text{C-thin}}$ is the fraction ($= 0.19_{-0.03}^{+0.04}$) of the “leaked” direct AGN emission, $N_{\text{H, nuclear HMXB}} \times PL_{\text{nuclear HMXB}}$ is the highly obscured emission from HMXBs in the nucleus, $N_{\text{H, host HMXB}} \times PL_{\text{host HMXB}}$ is the emission from HMXBs outside of the nucleus (only detected in annulus #3), line[1 – 4] are Gaussian fits to the emission lines, and Nebula = MEKAL₁ + MEKAL₂ or vpshock to reproduce the emission from the hot diffuse gas (vpshock is a constant temperature, plane-parallel shock plasma model; e.g., Borkowski, Lyerly, & Reynolds 2001).

⁵Note that the *Chandra* data used by Teng et al. (2014) is much shallower than what we use here since Teng et al. (2014) only used the *Chandra* data that were strictly simultaneous with the NuSTAR observations – less than 50 ksec – to avoid issues associated with AGN variability.

3.2.1. Radial Profile

The annular spectral extraction regions were defined in the following fashion: (1) Nucleus - defined to be $R < 1.0$ kpc ($\sim 1''15$). This is a conservatively large radius to make sure that most of the nuclear emission is included in this region (see Figure 2). (2) Annulus #1 (1.0 – 2.0 kpc) - this corresponds to the outflow region from RV11, approximately matching the radial extent of the Na I D outflow, but avoiding the bright star-forming arc to the south. (3) Annulus #2 (2.0 – 6.0 kpc) - this corresponds to the host galaxy region and includes all of the emission from the southern star-forming arc. The outer radius was chosen to include only the portion of the nebula where the PSF wings of the central AGN still contribute to the hard X-ray flux. This region also corresponds roughly with the brighter, more relaxed portion of the merger remnant (e.g., Veilleux et al. 2002, 2006). (4) Annulus #3 (6.0 – 16.0 kpc) - the outer radius corresponds roughly to the optical edge of the merger remnant. (5) Annulus #4 (16.0 – 40.0 kpc) - this includes all of the soft X-ray emission that is outside of the optical remnant but still largely within the optical tidal complex shown in Koda et al. (2009).

The extracted X-ray spectra and their best-fit models are shown in Figure 5 and the derived properties are listed in Table 2. The shapes of the spectra show a significant dependence on radial distance, confirming the radial gradient in the hardness ratio displayed in Figures 2 – 3. Our best-fit models translate this hardness ratio gradient into a radial dependence on the intensity of the central AGN component, consistent with the expected PSF and our image analysis (§3.1), relative to the soft X-ray emission from the extended nebula. The drop in hardness ratio with increasing radial distance from the nucleus out to annulus #2 is due entirely to this effect. In annulus #3 ($R = 6 - 16$ kpc), the flux from the PSF wings of the central AGN is negligible, yet hard (> 2 keV) X-rays are still detected. The high-energy portion of this spectrum was fitted using a cutoff power-law component meant to represent the HMXBs from circumnuclear star-forming regions. The implied SFR in this annulus is $\sim 10 M_{\odot} \text{ yr}^{-1}$. This component is not needed in the outer halo (annulus #4). The soft X-ray continuum emitted by the nebula is fit equally well with thermal (MEKAL) and shock models (all have $\chi^2/\text{d.o.f.} \lesssim 1.1$; see notes to Tables 2a and 2b). The thermal models require a second MEKAL component with lower temperature (0.27 keV) to reproduce the softer spectra beyond $R = 6$ kpc (annuli #3 and #4). The absence of a low-temperature MEKAL component inside of 6 kpc may be due to extra heating in this region from the circumnuclear star formation, the central quasar activity, and/or the galactic-scale AGN-driven outflow. We return to this issue in the next section, where we examine the azimuthal spectral variations in the inner region of Mrk 231.

The spectra in Figure 5 were also examined for absorption and emission features. No

obvious sign of O VII 0.7 keV and O VIII 0.9 keV absorption edges is seen in any of these spectra. To quantify this statement, we added an edge at 0.7 keV and another one at 0.9 keV in the fits to simulate the O VII and O VIII features, respectively. The difference in χ^2_ν was found to be insignificant (0.01 for two degrees of freedom). The tentative detection of the 0.7 keV warm absorber in the 2000 *Chandra* spectrum of the nucleus of Mrk 231 (Figure 9 of Gallagher et al. 2002) is therefore not confirmed here despite the factor of ~ 2 smaller uncertainties on the equivalent width measurements. However, a number of emission lines are present and provide constraints on the temperature and abundances of O, Mg, Si, and Fe in the nebula (using the abundances of Wilms, Allen, & McCray 2000). The features around 1.3 and 1.9 keV are identified as Mg XI 1.352 keV and Si XIII 1.864 keV, respectively. Both of these features are present outside of the nucleus: the Si XIII line is detected in the spectra of annuli #1, #2, #3, and #4, while Mg XI is convincingly detected in annuli #3 and #4. In the nuclear spectrum, there are also two lines near 6.4 and 6.7 keV with relatively small equivalent widths, consistent with previous data (e.g., Teng & Veilleux 2010) and the new analysis of Teng et al. (2014). These two lines are neutral or weakly ionized Fe K α and He-like Fe XXV K α , respectively. The Fe XXV 6.7 keV line may also be present outside of the nucleus (Figure 5). We return to this point in §3.2.5, where we present narrowband line images derived from our data.

Overall, the results of the fits listed in Table 2 suggest subsolar Fe abundances and solar or supersolar Si abundances throughout the nebula (particularly in the inner region; annulus #1), while O and Mg abundances fall between these two extremes. These abundances apply only to the dominant ($\sim 90\%$) warmer thermal component of the halo. The abundances of the cooler component could not be constrained separately because this component is too faint. In Table 2, the abundances of the cooler component were fixed to those of the warmer component. The absolute values of these abundances should be treated with caution [e.g., Kim 2012; although our use of a two-temperature model to fit the halo spectra should reduce the so-called “Fe bias” (Buote & Fabian 1998; Buote 2000)], as implied by the large error bars on these measurements in Table 2. However, the relative abundances are considerably more robust. The relative abundances of the α -elements (Si, O, and Mg) with respect to iron are $\sim 2 - 4 \times$ solar. Similar supersolar α -element abundances were recently found in the warm thermal component of the halo of NGC 6240 (Nardini et al. 2013), a galaxy merger that is caught in the pre-coalescence stage, i.e. at an earlier stage of evolution than Mrk 231. We discuss the implications of these results in §4.2.

3.2.2. Neutral Outflow Region

The spatially resolved Na ID outflow detected by Rupke et al. (2005c) and mapped by RV11 and RV13 extends to at least $\sim 2.0 - 2.5$ kpc, depending on azimuth angle. There is a region $\sim 1.0 - 2.5$ kpc due north from the nucleus of Mrk 231 where the Na ID outflow velocities are noticeably higher than along other directions (see right panels in Figure 4 of RV11). RV11 argue that the outflowing neutral gas in this region may be given an extra kick by the radio jet, seen on smaller scale along this same direction (e.g., Carilli et al. 1998; Ulvestad et al. 1999). With this in mind, we extracted spectra from four separate quadrants within annulus #2 ($R = 1.0 - 2.0$ kpc): one coinciding roughly with the possibly jet-influenced region ($PA = -45 - +45^\circ$) and three other regions of the same radial and azimuthal extent but due east, south, and west ($PA = 45 - 135, 135 - 225, \text{ and } 225 - 315^\circ$, respectively). Note that the radial extent of these regions was limited to 2.0 kpc, instead of 2.5 kpc, to avoid contaminating emission from the star-forming arc beyond 2 kpc which would affect the spectra in the southern comparison region.

The fact that these spectral regions are at the same distance from the nucleus eliminates any effects that may be due to the radial gradient of the hardness ratio associated with the wings of the AGN component discussed in the previous section. The four spectra were binned to at least 25 counts per bin and fitted simultaneously. We used the same fitting method here as that used for the annular regions, fitting all four spectra simultaneously. As in §3.2.1, the soft X-ray emission was modeled using either a single thermal MEKAL component with fixed kT or a single shock component with fixed kT . The strength of this soft component was left as a free parameter to reflect variations between the various regions, while the flux from the wings of the PSF was held fixed. The results are shown in Figure 6 and tabulated in Table 3 for the various models.

The hardness ratios tabulated in Table 3 indicate that the emission from the eastern quadrant is slightly softer than that from the other three regions. RV11 and RV13 have pointed out the presence of a prominent H II region ~ 1 kpc due east of the nucleus (see Figure 20 of RV13); this H II region likely contributes to the excess soft X-ray emission detected in the eastern spectrum. A fainter H II region may also be present in the northern quadrant (see the low-[N II]/H α “blob” in the middle top panel of Figure 20 of RV13) and may be contributing to the soft X-ray emission in this region, although the hardness ratio at that location is not significantly different from that in the western region. We see no evidence (e.g., higher temperatures in Table 3) for jet interaction with the ISM in the northern region. The spectral fits reveal the presence of a line at 1.9 keV in the eastern quadrant and perhaps also in the northern quadrant. This line is identified as Si XIII 1.864 keV. The fits require super-solar Si abundances that may reflect α -element enhancement from star formation at

these particular locations.

Most notably, the fits indicate a clear deficit of soft X-rays in the western outflow region. This region shows the faintest $H\alpha$ emission and some of the largest Na ID equivalent widths (Figures 20 and 18d of RV13, respectively). X-ray absorption by the column of neutral material at this location ($N_H \sim 10^{22} \text{ cm}^{-2}$ from RV13) may explain the weaker soft X-ray flux. Such photoelectric absorption would harden the soft X-ray spectrum by preferentially removing the softest X-rays and would thus translate into higher fit temperatures. To test this possibility, we searched for azimuthal temperature variations by allowing the temperature of the MEKAL component to vary for the fits in Table 3. In this case, all quadrants were assumed to have the same abundances, resulting in $\text{Si} = 4.7_{-2.3}^{+4.1}$ solar, $\text{Fe} = 0.3_{-0.2}^{+0.3}$ solar, and the other elements held fixed at solar. The resulting temperatures were $kT = 0.80_{-0.19}^{+0.27}$ keV, $0.70_{-0.20}^{+0.19}$ keV, $0.26_{-0.17}^{+0.42}$ keV, and $0.88_{-0.19}^{+0.29}$ keV for the eastern, southern, western, and northern regions, respectively (the temperature in the western region is harder to constrain due to the lower counts in this region). These numbers are all consistent with each other within the (rather large) uncertainties of these measurements. The deficit of soft X-rays in the western outflow region therefore appears to be intrinsic rather than due to photoelectric absorption by the neutral outflow. We return to this result in §4.1.

3.2.3. Southern Tidal Arc

Figure 4 shows the extraction windows used to characterize the X-ray emission from the arc and three comparison regions of the same size and radial extent (2.0 – 4.5 kpc) as the arc region but located at different position angles. The results of the spectral analysis are shown in Figure 7 and tabulated in Table 4. The soft X-ray emission in the western arc region is significantly weaker than in the other arc regions. In contrast, the hard X-ray emission is very nearly constant, resulting in a higher hardness ratio in the western region. This soft X-ray flux deficit is analogous to the behavior at smaller radii (§3.2.2) and may thus be physically related to the outflow.

The only other significant difference between these spectra is the detection of emission lines near ~ 1.8 keV and perhaps also at ~ 1.2 keV in the arc region but not in the other regions. These features are identified as Si XIII 1.864 keV and Ne X 1.211 keV (or Fe XIX 1.258 keV), respectively. This excess line emission may reflect α -element enhancement due to the starburst in the arc region.

3.2.4. Northern Tidal Tail

A polygonal extraction region (Figure 8) was used to extract the 0.5 – 2 keV spectrum in the region blocked by the northern tidal tail. The same polygonal footprint was used to extract a comparison spectrum in a region near the tidal tail, at approximately the same distance from the center. The best-fit model from annulus #4 is scaled to fit the comparison spectrum. Then an absorption component is added to the best-fit model, with increments of $\Delta N_H = 5 \times 10^{20} \text{ cm}^{-2}$ at a time, until the total 0.5 – 2 keV counts in the simulated spectrum correspond to the total counts from the region affected by the tidal tail. The hydrogen column density derived in this manner is $2.5 \times 10^{21} \text{ cm}^{-2}$. This column density is formally a lower limit since foreground emission would imply a larger column density. The value of this lower limit is slightly smaller than the column density derived by Iwasawa et al. (2011) in the tidal tail of Mrk 273, $6 \times 10^{21} \text{ cm}^{-2}$, but similar to the typical HI column density of an edge-on galaxy disk (e.g., Begeman 1989; Barber et al. 1996 have also made measurements of disk shadowing against the extragalactic X-ray background). This difference in column densities between the tidal tails of Mrk 231 and Mrk 273 may simply be an orientation effect: the tidal tail in Mrk 273 appears thinner, less diffuse than the northern tidal tail in Mrk 231, perhaps indicating a more edge-on orientation.

3.2.5. Narrowband Line Images

Guided by the detection of emission lines outside of the nucleus (Figures 5, 6, and 7), we extracted narrowband line images to investigate the two-dimensional spatial distribution of the line-emitting gas. The results for Si XIII 1.864 keV, neutral or slightly ionized Fe K α 6.4 keV, and the sum of He-like Fe XXV 6.7 keV and H-like Fe XXVI 6.9 keV are shown in Figure 9 (Mg XI 1.352 keV was too faint for this exercise). The derived strengths of the line emission are unreliable in the central 3.0 kpc diameter region due to Poisson noise from the very strong underlying AGN continuum; this region is therefore masked in all three panels of Figure 9.

We find clear evidence for Si XIII emission outside of the nucleus, extending at least ~ 5 kpc south of the nucleus. Some of the strongest Si XIII emission coincides with the southern star-forming arc, confirming the results from our spectral analysis (§3.2.3).

We do not find convincing evidence for Fe K α emission outside of the nucleus. The small extension to the north-west in the middle panel of Figure 9 is not statistically significant. A slightly more significant extension is seen in the Fe XXV 6.7 keV + Fe XXVI 6.9 keV line emission map (right panel). The spectrum extracted from a 2-arcsec diameter region centered

on the brightest part of that extension is shown in black in Figure 10. The spectrum in red is from an equal-size region on the opposite side of the nucleus where there is no obvious Fe XXV + Fe XXVI emission in the line emission map. There is a difference of 16 counts between these two spectra in the 0.5-7 keV band, but some of this excess in counts could be due to a slightly higher continuum level. A line seems to be present in the black spectrum but not in the red one. Formally the fit shown in Figure 10 gives $E(\text{line}) = 6.629_{-0.044}^{+0.063}$ keV, $EW(\text{line}) = 2.042_{-1.743}^{+1.693}$, and a narrow width ($\sigma = 0$ keV formally). This is thus a tentative detection of Fe XXV 6.7 keV outside of the nucleus.

The fits to the annular regions discussed in §3.2.3 (Figure 5, Table 2) suggested the presence of Fe XXV 6.7 keV in annulus #3 ($R = 6 - 16$ kpc), where the AGN does not contribute any continuum emission. This line emission is not immediately obvious in the Fe XXV + Fe XXVI emission map. The spectrum extracted from annulus #3 is shown in more detail in Figure 11 using a finer binning than in Figure 5. The best fit ($\chi^2_\nu = 1.18$) shown in this figure constrains the equivalent width of the Fe XXV 6.7 keV line to be $2.09_{-1.40}^{+1.94}$ keV. Given the large error bars, the detection of this line is thus again only tentative.

4. Discussion

4.1. The Quasar-Driven Wind of Mrk 231

The main objective of the new *Chandra* data set was to provide enough counts to allow us to carry out a detailed spectral imaging analysis of the galactic-scale outflow region. The results of this analysis were discussed in detail in §3.2. Everywhere in the nebula, we find that thermal (MEKAL) models fit the data equally well as simple shock models. The gas in the outer ($R > 6$ kpc) nebula is characterized by a dominant ($\sim 90\%$) thermal component at $kT \sim 0.7$ keV and a fainter ($\sim 10\%$) component at $kT \sim 0.3$ keV. The cooler component is not present in the inner ($R < 6$ kpc) region. No sign of O VII 0.7 keV and O VIII 0.9 keV absorption edges (“warm absorbers”) is found in any of the spectra, further indicating the absence of cool gas in the central region of Mrk 231. This result is somewhat surprising since warm absorbers are ubiquitous in Seyferts (e.g., Crenshaw et al. 2003) and QSOs (e.g., Piconcelli et al. 2005; Teng & Veilleux 2010).

A more detailed study of the outflow region, where we sliced the annular region between $R = 1$ and 2 kpc into four equal-size quadrants (N, S, E, and W), reveals significant variations in hardness ratios and intensities. The spectrum in the eastern outflow region is found to be significantly softer and shows a larger Si/Fe abundance ratio than the other outflow regions. This is likely due to the presence of an HII region visible in the optical data (RV13). A

fainter HII region may also be affecting the spectrum in the northern quadrant. A deficit of soft X-ray emission is present in the western quadrant, coincident with fainter $H\alpha$ emission and some of the largest neutral-gas Na ID absorption columns. This is the strongest evidence in our data that the hot X-ray emitting gas “knows” about the massive neutral outflow in this object. There is also tentative evidence for Fe XXV 6.7 keV line emission extending up to ~ 3 kpc north-west of the nucleus, but this is only a 2-sigma detection so it is not very significant (Figures 9 – 10).

It is perhaps surprising that our data do not show any obvious temperature enhancements in the neutral outflow region given that the velocities of the outflowing neutral gas are typically ~ 1000 km s $^{-1}$. One would naively expect this neutral outflow to interact with the ambient ISM and produce strong ionizing shocks. For non-radiative, strong shocks in a fully ionized monoatomic gas, the post-shock temperature $T_{sh} = 3\mu v_{sh}^2/16k$, where μ is the mean mass per particle and k is the Boltzmann constant (McKee & Hollenback 1980). For shock velocities of ~ 1000 km s $^{-1}$, we expect hot gas with $T \sim 1.6 \times 10^7$ K or $kT \sim 1.40$ keV. The tentative detection of extended Fe XXV 6.7 keV emission would imply shock velocities of $\gtrsim 2000$ km s $^{-1}$, if produced by a collisionally ionized plasma with a temperature $T \sim 7 \times 10^7$ K as in NGC 6240 (Wang et al. 2014). These high velocities are not seen in the neutral gas. Our fits do not formally rule out the possibility that HMXBs at this location may be responsible for this extended Fe XXV emission.

These simple back-of-the-envelope arguments emphasize the fact that one has to be very cautious when using the properties of the neutral outflow to predict those of the hot X-ray emitting material. This may not be too surprising given the huge disparity in temperatures (< 1000 K versus $\sim 10^7$ K) and densities (> 1 cm $^{-3}$ versus $\sim 10^{-2}$ cm $^{-3}$; Table 3) between these two gas phases. It would be more prudent to compare the properties of the X-ray emitting gas with those of the warm ionized gas traced by $H\alpha$, which is often found to be spatially correlated with the soft X-ray emission (e.g., Cecil, Bland-Hawthorn, & Veilleux 2002; Strickland et al. 2004; Bolatto et al. 2013). Unfortunately, contaminating $H\alpha$ emission from HII regions complicates the picture in Mrk 231 and the $H\alpha$ outflow is detected convincingly only within ~ 1 kpc (RV13). Indeed, all of the evidence (RV11, RV13, Fischer et al. 2010; Feruglio et al. 2010; Gonzalez-Alfonso et al. 2014) suggests that the outflow of Mrk 231 is heavily mass-loaded with neutral and molecular material but relatively little ionized gas; our new *Chandra* data add support to this idea. The absence of hot-shocked ionized gas in the wind region naively suggests that the outflow is momentum-driven rather than energy-driven. However, this is not a strong conclusion since we cannot strictly rule out the presence of a very hot ($>> 10^7$ K) and tenuous wind fluid gas (present in the energy-driven wind of M82; Griffiths et al. 2000; Stevens, Read, & Bravo-Guerrero 2003).

The absence of the cooler thermal component within ~ 6 kpc indicates either more efficient cooling on large scale or additional heating on small scale. Adiabatic expansion of a free wind can naturally explain negative temperature gradients but, as we just mentioned, there is very little evidence that any of the soft X-ray emitting gas detected within ~ 6 kpc is directly associated with the wind event. Moreover, there is no evidence at present that the galactic wind in Mrk 231 extends beyond ~ 3 kpc (RV11, RV13), let alone >6 kpc (note however that this is purely a limitation of the current optical data: Na ID absorption is not detected beyond ~ 3 kpc because the galaxy continuum is too faint). Even if the wind did extend beyond 6 kpc, it is not clear how the wind scenario could explain the presence of the (dominant) warmer component on the largest scale (out to ~ 25 kpc from the nucleus). Finally, the drop in X-ray surface brightness in Figure 2 is also less steep than the $\sim R^{-3}$ profile expected in the case of a freely expanding wind (where the gas and electron density profiles n_g and n_e go as $\sim r^{-2}$, from mass conservation, and the X-ray surface brightness $\Sigma_X \sim n_e^2 dV/dS$, where dV stands for the volume element and dS is the surface element). We therefore favor the scenario where the absence of the cooler component within 6 kpc is due to extra heating.

Known sources of heating in this region include the galactic-scale wind, the circumnuclear starburst, and the quasar itself. We discuss each in turn. The total kinetic energy of the AGN-driven galactic-scale outflow in Mrk 231 is substantial ($\sim 6 \times 10^{57}$ ergs) and dominated by the contributions from the neutral and molecular components (RV11, RV13, Feruglio et al. 2010, Cicone et al. 2012, and Gonzalez-Alfonso et al. 2014). For comparison, the *total* thermal energy of the X-ray emitting gas in the inner ($R < 6$ kpc) region of Mrk 231 is $3\eta n_e V kT \approx 10^{57}$ ergs, where we used a filling factor $\eta \sim 1$ (volume-filling), an electron density $n_e \sim 2 \times 10^{-2} \text{ cm}^{-3}$ (Table 3; $\propto \eta^{-1/2}$), a spherical volume $V \sim 2.4 \times 10^{67} \text{ cm}^3$, and a temperature of $8 \times 10^6 \text{ K}$ (0.7 keV). The absence of cooler (~ 0.3 keV) X-ray emitting gas in the inner region of Mrk 231 may therefore be due to the influence of the AGN-driven outflow on the ambient ISM, even if only a small fraction of this kinetic energy is thermalized via shocks (e.g., Cox et al. 2006). However, the lack of a clear signature of ionizing shocks in the neutral outflow region and the current size limits on this outflow ($\gtrsim 3$ kpc) weaken this wind scenario.

The star formation rate of Mrk 231 is $\sim 140 M_\odot \text{ yr}^{-1}$ (Veilleux et al. 2009). This starburst therefore injects mechanical energy in the surrounding medium at a rate $\sim 1 \times 10^{44} \text{ erg s}^{-1}$ (e.g., Veilleux et al. 2005). The age of this starburst is not well constrained. Assuming a conservatively small value of 5×10^6 yrs for the starburst age, the starburst can contribute up to 10^{57} ergs if the thermalization efficiency is $>10\%$. This is more than enough to explain the lack of a cool component in the inner 6 kpc. However, there is no evidence that the starburst extends much beyond ~ 3 kpc, except in the southern tidal arc where the

starburst may be blowing its own low-velocity wind (RV11, RV13).

The bolometric luminosity of the quasar in Mrk 231 is $\sim 3 \times 10^{12} L_{\odot}$ (Veilleux et al. 2009), but most of this energy is emitted in the infrared and cannot contribute to heating the hot X-ray emitting gas in the inner 6 kpc of the nucleus. The recent *NuSTAR* data of Teng et al. (2014) indicate that Mrk 231 is underluminous in the X-rays with an intrinsic absorption-corrected 0.5 – 30 keV luminosity of $1.0 \times 10^{43} \text{ erg s}^{-1}$. Assuming a quasar lifetime of $10^7 - 10^8$ yrs (see, e.g., review by Martini 2004), only $\sim 2 - 20\%$ of the 0.5 – 30 keV total energy output from the quasar in Mrk 231 needs to be absorbed within the inner 6 kpc of the quasar to contribute $\sim 10^{57}$ ergs to the heating of the inner region. The analysis of the *NuSTAR* data indicates that a patchy and Compton-thin ($N_H \sim 1.12_{-0.24}^{+0.29} \times 10^{23} \text{ cm}^{-2}$) column absorbs (1 - C-thin) = $\sim 80\%$ of the intrinsic 0.5 – 30 keV luminosity of the quasar in Mrk 231. Assuming that our line of sight to the quasar is typical of other directions, this energy is amply sufficient to explain the lack of a cool component in the inner 6 kpc of Mrk 231. However, this energy is not deposited at the right place. The absorbing column measured by *NuSTAR* is spatially unresolved (< 1 kpc) so the energy absorbed by this material is deposited on a scale considerably smaller than 6 kpc. Perhaps some fraction of the quasar energy output that makes it out of the nucleus is absorbed by material on $> \text{kpc}$ scale, including possibly the neutral atomic and molecular gas entrained in the wide-angle outflow (large-scale ionization is seen in the circumgalactic nebula of MR2251–178 for instance; Kreimeyer & Veilleux 2013). Another possibility is that the energy deposited on sub-kpc scale is redistributed on larger scales via slower dynamical processes, e.g., buoyant bubbles of hot gas mixing with the cooler X-ray material, as seen in the intracluster medium of a growing number of galaxy clusters (e.g., Hlavacek-Larrondo et al. 2012).

Our current data set does not allow us to discriminate between heating by the galactic wind, the circunuclear starburst, and the quasar. Most likely, all three contribute at some level to the absence of the cool thermal component within ~ 6 kpc.

4.2. Origin of the X-ray Halo

The spectacular X-ray halo in Mrk 231 has many properties that are similar to those of the halo in NGC 6240 (Nardini et al. 2013), a galaxy merger at an earlier stage of evolution than Mrk 231. We argue below that they likely have similar origins.

The total luminosity of the nebula around Mrk 231 is $\sim 2 \times 10^{41} \text{ erg s}^{-1}$ (annuli #1 – #4 in Table 2, excluding the contribution from the wings of the AGN PSF and host HMXBs), similar to that of the halo in NGC 6240 and, as pointed by Nardini et al. (2003), comparable

to that of small groups of galaxies (Mulchaey 2000) and giant ellipticals (Canizares et al. 1987; Mathews & Brighenti 2003). The full halo spectrum of NGC 6240 calls for two thermal (MEKAL) components with temperatures $kT \sim 0.8$ and 0.25 keV, while our best-fit model for the halo in Mrk 231 involves two thermal components with $kT \sim 0.7$ keV and ~ 0.3 keV with the latter component contributing only $\sim 10\%$ of the luminosity. Given the smaller dimensions of the nebula around Mrk 231 ($\sim 65 \times 50$ kpc) relative to that of NGC 6240 ($\sim 110 \times 80$ kpc), the sound-crossing time, $D/c_s = D(5kT/3\mu m_p)^{-1/2}$, a rough measure of the dynamical age of the halo, is proportionally smaller in Mrk 231: ~ 100 Myr versus ~ 200 Myr. The thermal energy content of the halo in Mrk 231, $E_{th} \sim 2 \times 10^{58}$ erg, is also slightly smaller than that of the halo in NGC 6240 ($\sim 5 \times 10^{58}$ erg), but still considerable if we compare it to the amount of kinetic energy deposited during the merger of two identical progenitors, of order $M_g v_c^2/8$, where M_g is the mass of the X-ray emitting gas and v_c is the relative speed during the collision (Nardini et al. 2013). In the case of Mrk 231, $M_g = \eta n_e V m_p \sim 7 \times 10^9 M_\odot$ so $v_c \sim 1400$ km s $^{-1}$ is needed, which is substantially faster than typical head-on collisions in non-cluster environments (e.g., Taffy Galaxies; Braine et al. 2003). A comparison of the thermal energy content of the halo in Mrk 231 with its X-ray luminosity implies a cooling timescale $\sim 10^{17}$ sec or ~ 3 Gyr.

As discussed in §4.1, the present-day starburst, AGN, and galactic wind in the core of Mrk 231 no doubt have injected some energy in the X-ray nebula and may be responsible for the absence of cool gas in the inner (< 6 kpc) region of the nebula. But, they are unlikely to have supplied the entire thermal energy content of the X-ray halo given the energetics of these processes (see §4.1). The large size of the nebula also puts severe constraints on the duration of these events: e.g., $\gtrsim 100$ Myr for an average velocity of $\lesssim 500$ km s $^{-1}$, which seems at odd with the starburst age ($< 10^7$ yrs) and the dynamical age of the present-day galactic wind (a few $\times 10^6$ yrs).

Independent constraints on the processes at work come from our abundance analysis of the halo (annuli #3 and #4 in §3.2.1; Tables 2a and 2b). We measure α -element (particularly Si, but also O and Mg) abundances relative to iron that are $\sim 2 - 4 \times$ solar throughout the nebula without significant radial gradient. A similar abundance pattern was found in the halo of NGC 6240 (Nardini et al. 2013). Iron is mainly produced from type Ia supernovae (SNe; i.e., exploded white dwarfs in close binary systems) on a timescale of $\sim 0.1-1$ Gyr, while the α -elements come primarily from type II SNe (i.e., core-collapsed massive stars) on timescales of a few tens of Myr. Synthesis models for Type II SNe (e.g, Heger & Woosley 2010; Nomoto et al. 2006, 2013) predict Si/Fe ratios of up to $\sim 3-5$ solar, while ratios of ~ 0.5 solar are expected from Type Ia SNe (e.g., Nagataki & Sato 1998; Seitzzahl et al. 2013). The supersolar Si/Fe ratios in the halos of Mrk 231 and NGC 6240 therefore suggest uniform enrichment by type II SNe out to the largest scales ($\sim 65 \times 50$ kpc in the case of

Mrk 231 and 110×80 kpc for NGC 6240). Supersolar Si/Fe ratios have been found in the past [e.g., face-on spiral galaxies (Schlegel et al. 2003; Soria & Wu 2003), galaxy mergers like the Antennae (Baldi et al. 2006a, 2006b), and the central regions of young elliptical galaxies with sites of recent (a few tens of Myr) merger-induced star formation (Kim et al. 2012)], but in all of these cases, the supersolar Si/Fe ratios are measured on kpc scale, not several tens of kpc as in Mrk 231 and NGC 6240.

In Mrk 231, we see evidence for α -element enhancements near and around the circumnuclear starburst (§3.2.2) but the on-going (age $< 10^7$ yrs) episode of active star formation ($SFR \sim 140 M_{\odot} \text{ yr}^{-1}$) does not seem capable of explaining the large-scale enhancements seen in the halo. The estimated mass in silicon in the halo is $\sim 6 \times 10^6 M_{\odot}$, assuming a solar silicon abundance (Table 2a). The maximum silicon yield of type II SNe is $\sim 0.1 - 0.3 M_{\odot}$ for a massive-star progenitor with $Z \leq 0.02$ (e.g. yields tables in Nomoto et al. 2013) and thus implies the need for $\sim 3 \times 10^7$ type II SNe or a sustained star formation rate of $\sim 140 M_{\odot} \text{ yr}^{-1}$ over $\geq 10^7$ yrs. Moreover, the metals produced in the circumnuclear starburst need to be redistributed over the entire $\sim 55 \times 60$ kpc nebula to be consistent with the observations. In some cases, there is direct evidence that galactic winds help carry the α -element enhanced material produced by starburst into the halos of galaxies (e.g., M82: Tsuru et al. 2007; Ranalli et al. 2008; Konami et al. 2011 and references therein), but the present-day galactic wind in Mrk 231 cannot be responsible for the supersolar Si/Fe ratios throughout the halo of Mrk 231 unless the wind actually extends ~ 1 order of magnitude further than currently measured ($\gtrsim 3$ kpc, RV11, RV13). Another, more likely, scenario is that the α -elements produced near the center have been redistributed on larger scale by previous outflow events.

In NGC 6240, the warmer ($kT_1 \sim 0.8$ keV) component of the halo is distinctly metal-richer ($Z_{\alpha} \sim 0.5$ solar) than the cooler ($kT_2 \sim 0.25$ keV) component (fixed at $Z = 0.1$ solar). Nardini et al. (2013) associate the first component with chemically-evolved, starburst-processed gas and the second component with gravitationally-bound, pre-existing halo material. The cooler halo component in Mrk 231 is $\sim 10\times$ weaker than the warmer component so, unfortunately, our *Chandra* data do not have sufficient counts to constrain the metal abundance in this fainter component, hence its origin⁶. However, regardless of the exact origin of the cooler halo component in Mrk 231, we mentioned in the previous paragraph that the sheer amount of metals in the warmer component and its widespread supersolar Si/Fe ratios point to enhanced star formation over timescales comparable to the dynamical time (~ 100 Myr) to both produce these metals and redistribute them across the halo via outflow

⁶For instance, we determined that models with a low metal abundance of $Z = 0.1$ solar in the cooler component fit the data equally well as models with $Z = 1$ solar.

events. The merger itself may also help in redistributing the metals. Mrk 231 is in the throes of a major merger of two gas-rich disk galaxies with masses similar those of the Milky Way and Andromeda (Cox & Loeb 2008). The colliding gas in the parent disk galaxies of the merger is shock-heated to X-ray-emitting temperatures and eventually mixed with the pre-existing halo material to contribute to the observed X-ray halo (Jog & Solomon 1992; Cox et al. 2006). The lack of systematic Si/Fe ratio variations across the halo of Mrk 231 suggests that the collision and outflow events were efficient at erasing abundance gradients.

Some fraction of the X-ray gas present in the halo of Mrk 231 will likely be retained by the merger remnant and become the X-ray-emitting halo of the resulting young elliptical galaxy. While solar Si/Fe ratios are typically seen in the X-ray halos of present-day large elliptical galaxies (e.g., Humphrey & Buote 2006; Loewenstein & Davis 2010, 2012; Konami et al. 2014), supersolar Si/Fe ratios are often measured in the stellar components of $>L^*$ ellipticals (e.g., Worthey 1998; Graves et al. 2010; Conroy et al. 2014). The stellar abundances are generally explained by invoking a short timescale of star formation (efficient quenching before the onset of type Ia SNe) or variations in the IMF. Given the mass outflow rate and gas content of Mrk 231, the implied gas depletion time scale is only 10 – 20 Myr (Sturm et al. 2011; Gonzalez-Alfonso et al. 2014). The outflow in Mrk 231 could thus quench star formation on this short time scale, if the ejected gas does not return to the center to form stars. This type of life-changing outflow event appears to be common among local ULIRGs (Veilleux et al. 2013; Spoon et al. 2013; Ciccone et al. 2014). Assuming Mrk 231-like outflow events are also common in major mergers in the early universe, they might help explain the enhancement of α -element, relative to iron, observed in the stellar population of local large elliptical galaxies.

5. Conclusions

We have combined a deep 400-ksec ACIS-S observation of Mrk 231 with 120-ksec archival data acquired with the same instrument and setup to allow us to carry out the first spatially resolved spectral analysis of a hot X-ray emitting circumgalactic nebula around a quasar. Mrk 231 is particularly well suited for this study since it is the nearest quasar and is well known to host a powerful galactic-scale outflow. The main results from our study are the followings:

- The morphology of the $\sim 65 \times 50$ kpc X-ray nebula does not resemble that of the tidal complex of Mrk 231 seen at optical wavelengths. The only spatial match is the small tidal arc located ~ 3.5 kpc south of the nucleus, where excess soft X-ray continuum emission and Si XIII 1.8 keV line emission are detected, consistent with star formation

and its associated α -element enhancement, respectively. We also detect a deficit in the soft X-ray flux map at the position of the northern tidal tail, suggesting that this structure casts an X-ray shadow due to a hydrogen column density of at least $2.5 \times 10^{21} \text{ cm}^{-2}$.

- The soft X-ray spectrum of the nebula beyond 6 kpc is best described as the sum of two thermal components of temperatures ~ 3 and ~ 8 million K with spatially uniform super-solar α element abundances, relative to iron. A similar result was recently found in the X-ray halo of the pre-merger NGC 6240. Enhanced star formation activity over an extended period of time ($\sim 10^8$ yrs) is needed to produce the vast amount of α elements detected in the nebula of Mrk 231. Multiple outflow events, such as the on-going quasar-driven galactic wind, may help carry the α elements produced in the circumnuclear region out to the largest scales. Such wind-driven metal transport is directly seen to take place in the nearby starburst M 82, albeit on a considerably smaller scale. The stirring of the gas associated with the merger itself may also redistribute the metals across the nebula and help erase remaining abundance gradients.
- The hard X-ray continuum emission in the inner (≤ 6 kpc) nebula is consistent with being due entirely to the bright central quasar and the wings of the *Chandra* point spread function. The ~ 3 million K thermal component detected in the halo is not present within 6 kpc of the nucleus. No sign of O VII 0.7 keV and O VIII 0.9 keV absorption edges (“warm absorbers”) is found in any of the spectra, further indicating a lack of cool X-ray detectable gas in the central region of Mrk 231. Energetically, heating from the circumnuclear starburst, the central quasar activity, or the wide-angle quasar-driven outflow is each capable of explaining this lack of cool gas. The strongest evidence in our data that the hot X-ray emitting gas “knows” about the massive neutral/molecular outflow in this object is a deficit of soft X-ray emission in the western quadrant extending 1 – 2 kpc (perhaps as far as 2 – 4.5 kpc) from the nucleus. This region coincides with fainter $H\alpha$ emission and some of the largest columns of outflowing neutral gas probed by observations of the Na I optical doublet. Shocks created by the interaction of the wind with the ambient ISM may heat the gas to high temperatures at this location. Indeed, there is tantalizing ($2\text{-}\sigma$) evidence for Fe XXV 6.7 keV line-emitting gas extending up to ~ 3 kpc north-west of the nucleus. If produced by a collisionally ionized plasma with a temperature $T \sim 7 \times 10^7$ K, as in the case of NGC 6240, this would imply shock velocities $\gtrsim 2000 \text{ km s}^{-1}$. HMXBs may also be responsible for this extended line emission.

We thank the anonymous referee for thoughtful and constructive comments that improved this paper. Support for this work was provided by NASA through *Chandra* contract GO2-13129X (S.V.) and the NASA Postdoctoral Program (NPP) Fellowship (S.H.T., S.V.). S.V. acknowledges support from the Alexander von Humboldt Foundation for a “renewed visit” to Germany, and thanks the host institution, MPE Garching, where a portion of this paper was written. He is also grateful to R. Mushotzky for discussions of the interpretation of the elemental abundances. This work has made use of NASA’s Astrophysics Data System Abstract Service and the NASA/IPAC Extragalactic Database (NED), which is operated by the Jet Propulsion Laboratory, California Institute of Technology, under contract with the National Aeronautics and Space Administration.

REFERENCES

- Aalto, S., et al. 2012, *A&A*, 537, 44
- Baldi, A., et al. 2006a, *ApJS*, 162, 113
- Baldi, A., et al. 2006b, *ApJ*, 636, 158
- Barber, C. R., Roberts, T. P., & Warwick, R. S. 1996, *MNRAS*, 282, 157
- Begeman, K. G. 1989, *A&A*, 223, 47
- Boksenberg, A., et al. 1977, *MNRAS*, 178, 451
- Bolatto, A. D., et al. 2013, *Nature*, 499, 450
- Borkowski, K. J., Lyerly, W. J., & Reynolds, S. P. 2001, *ApJ*, 548, 820
- Boroson, T. A., et al. 1991, *ApJ*, 370, L19
- Braine, J., et al. 2003, *A&A*, 408, L13
- Braito, V., et al. 2004, *A&A*, 420, 79
- Buote, D. A., & Fabian, A. C. 1998, *MNRAS*, 296, 977
- Buote, D. A. 2000, *MNRAS*, 311, 176
- Canizares, C. R., Fabbiano, G., & Trinchieri, G. 1987, *ApJ*, 312, 503
- Carilli, C. L., Wrobel, J. M., & Ulvestad, J. S. 1998, *AJ*, 115, 928
- Cecil, G., Bland-Hawthorn, J., & Veilleux, S. 2002, *ApJ*, 576, 745
- Cicone, C., et al. 2012, *A&A*, 543, 99
- Cicone, C., et al. 2014, *A&A*, 562, 21
- Conroy, C., Graves, G. J., & van Dokkum, P. G. 2014, *ApJ*, 780, 33
- Cox, T. J., & Loeb, A. 2008, *MNRAS*, 386, 461
- Cox, T. J., et al. 2006, *ApJ*, 643, 692
- Crenshaw, M., Kraemer, S. B., & George, I. M. 2003, *ARA&A*, 41, 117
- Davies, R. I., Tacconi, L. J., & Genzel, R. 2004, *ApJ*, 613, 781
- Dermer, C. D., et al. 1997, *ApJ*, 484, L121
- Dickey, J. M., & Lockman, F. J. 1990, *ARA&A*, 28, 215
- Di Matteo, T., Springel, V., & Hernquist, L. 2005, *Nature*, 433, 604
- Downes, D., & Solomon, P. M. 1998, *ApJ*, 507, 615
- Eales, S. A., & Arnaud, K. A. 1988, *ApJ*, 324, 193

- Esch, D. N., et al. 2004, *ApJ*, 610, 1213
- Feruglio, C., et al. 2010, *A&A*, 518, L155
- Fischer, J., et al. 2010, *A&A*, 518, L41
- Forster, K., Rich, R. M., & McCarthy, J. K. 1995, *ApJ*, 450, 74
- Gallagher, S. C., et al. 2002, *ApJ*, 569, 655
- Gallagher, S. C., et al. 2005, *ApJ*, 633, 71
- Garmire, G. P., et al. 2003, *SPIE*, 4851, 28
- Gonzalez-Alfonso, E., et al. 2014, *A&A*, 561, 27
- Graves, G., J., Faber, S. M., & Schiavon, R. P. 2010, *ApJ*, 721, 278
- Grimes, J. P., et al. 2005, *ApJ*, 628, 187
- Hamilton, D., & Keel, W. C. 1987, *ApJ*, 321, 211
- Heger, A., & Woosley S. E. 2010, *ApJ*, 724, 341
- Hlavacek-Larrondo, J., et al. 2012, *MNRAS*, 421, 1360
- Humphrey & Buote, D. A. 2006, *ApJ*, 639, 136
- Hutchings, J. B., & Neff, S. G. 1987, *AJ*, 92, 14
- Iwasawa, K., et al. 2011, *A&A*, 528, 137
- Jog, C. J., & Solomon, P. M. 1992, *ApJ*, 387, 152
- Karovska, M., et al. 2005, *ApJ*, 623, L137
- Kashyap, V., et al. 2011, *Chandra Interactive Analysis of Observations (CIAO)*, Sec. 4.3
- Kim, D.-W. 2012, *Astrophysics and Space Science Library*, 378, 121
- Kim, D.-W., Fabbiano, G., & Pipino, A. 2012, *ApJ*, 751, 38
- Koda, J., et al. 2009, “The Starburst-AGN Connection”, *ASP Conference Series*, Vol. 408, Ed. W. Wang, Z. Yang, Z. Luo, and Z. Chen, p. 22
- Kollatschny, W., Dietrich, M., & Hagen, H. 1992, *A&A*, 264, L5
- Konami, S., Matsushita, K., Tsuru, T. G., Gandhi, P., & Tamagawa, T. 2011, *PASJ*, 63, 913
- Konami, S., Matsushita, K., Nagino, R., & Tamagawa, T. 2014, *ApJ*, 783, 8
- Kreimeyer, K., & Veilleux, S. 2013, *ApJ*, 772, L11
- Li, J., et al. 2004, *ApJ*, 610, 1204
- Loewenstein, M., & Davis, D. 2010, *ApJ*, 716, 384

- Loewenstein, M., & Davis, D. 2012, *ApJ*, 757, 121
- Lucy, L. B. 1974, *AJ*, 79, 745
- Maloney, P. R., & Reynolds, C. S. 2000, *ApJ*, 545, L23
- Mathews, W. G., & Brighenti, F. 2003, *ARA&A*, 41, 191
- McKee, C. F., & Hollenbach, D. J. 1980, *ARA&A*, 18, 219
- Murphy, K. D., & Yaqoob, T. 2009, *MNRAS*, 397, 1549
- Mulchaey, J. S. 2000, *ARA&A*, 38, 289
- Murray, N., Quataert, E., & Thompson, T. A. 2005, *ApJ*, 618, 569
- Nagataki, S., & Sato, K. 1998, *ApJ*, 504, 629
- Nardini, E., et al. 2013, *ApJ*, 765, 141
- Nomoto, K., et al. 2006, *Nucl. Phys. A*, 777, 424
- Nomoto, K., Kobayashi, C., & Tominaga, N. 2013, *ARA&A*, 51, 457
- Piconcelli, E., et al. 2005, *A&A*, 432, 15
- Piconcelli, E., et al. 2013, *MNRAS*, 428, 1185
- Ptak, A., et al. 2003, *ApJ*, 592, 782
- Ranalli, P., Comastri, A., Origlia, L., & Maiolino, R. 2008, *MNRAS*, 386, 1464
- Read, A. M., & Ponman, T. J. 1998, *MNRAS*, 297, 143
- Rudy, R. J., Stocke, J. T., & Foltz, C. B. 1985, *ApJ*, 288, 531
- Rupke, D. S. N., & Veilleux, S. 2011, *ApJ*, 729, L27 (RV11)
- Rupke, D. S. N., & Veilleux, S. 2013, *ApJ*, 768, 75 (RV13)
- Rupke, D. S., Veilleux, S., & Sanders, D. B. 2002, *ApJ*, 570, 588
- Rupke, D. S., Veilleux, S., & Sanders, D. B. 2005a, *ApJS*, 160, 87
- Rupke, D. S., Veilleux, S., & Sanders, D. B. 2005b, *ApJS*, 160, 115
- Rupke, D. S., Veilleux, S., & Sanders, D. B. 2005c, *ApJ*, 632, 751
- Sanders, D. B., & Mirabel, I. F. 1996, *ARA&A*, 34, 749
- Schlegel, E. M., Holt, S. S., & Petre, R. 2003, *ApJ*, 598, 982
- Seitzzahl, I. R., et al. 2013, *MNRAS*, 429, 1156
- Smith, P. S., Schmidt, G. D., Allen, R. G., & Angel, J. R. P. 1995, *ApJ*, 444, 146
- Soria, R., & Wu, K. 2003, *A&A*, 410, 53

- Spoon, H. W. W., et al. 2013, ApJ, 775, 127
- Stevens, I. R., Read, A. M., Bravo-Guerrero 2003, MNRAS, 343, L47
- Strickland, D. K., et al. 2004, ApJS, 151, 193
- Sturm, E., et al. 2011, ApJ, 733, L16
- Surace, J., et al. 1998, ApJ, 492, 116
- Teng, S. H., & Veilleux, S. 2010, ApJ, 725, 1848
- Teng, S. H., et al. 2014, ApJ, in press
- Tsuru, T. G., et al. 2007, PASJ, 58, S269
- Turner, T. J. 1999, ApJ, 511, 142
- Turner, T. J., & Kraemer, S. B. 2003, ApJ, 598, 916
- Ulvestad, J., Wrobel, J. M., & Carilli, C. L. 1999, ApJ, 516, 127
- Veilleux, S., Cecil, G., & Bland-Hawthorn, J. 2005, ARA&A, 43, 769
- Veilleux, S., Kim, D.-C., & Sanders, D. B. 2002, ApJS, 143, 315
- Veilleux, S., et al. 2006, ApJ, 643, 707
- Veilleux, S., et al. 2009, ApJS, 182, 628
- Veilleux, S., et al. 2013a, ApJ, 764, 15
- Veilleux, S., et al. 2013b, ApJ, 776, 27
- Wang, J., et al. 2014, ApJ, 781, 55
- Wilms, J., Allen, A., & McCray, R. 2000, ApJ, 542, 914
- Worthey, G. 1998, PASP, 110, 888

Table 1. Two-Component β -Model Fits to the X-ray Surface Brightness Radial Profiles

Model Parameter	Inner Component	Outer Component
0.5–2 keV		
R_0	0.62	3.31
β	1.00	0.54
Amplitude	1421.61	7.88
χ^2_ν		1.94
2–7 keV		
R_0	0.55	0.03
β	1.00	0.31
Amplitude	2481.61	14.13
χ^2_ν		1.89

Table 2. a) Simultaneous Model Fit to the Annular Regions (MEKAL models)

Model Parameter ^a	Nucleus	Annulus 1	Annulus 2	Annulus 3	Annulus 4
Radial Distance (kpc)	<1.0	1.0–2.0	2.0–6.0	6.0–16.0	16.0–40.0
Hardness Ratio	0.260±0.008	-0.107 ± 0.028	-0.648 ± 0.025	-0.636 ± 0.020	-1.000 ^{+0.024} _{-0.000}
Ratio to Nuclear NuSTAR Model	0.8134 ^{+0.0132} _{-0.0137}	0.0409 ^{+0.0029} _{-0.0029}	0.0257 ^{+0.0026} _{-0.0026}	0 (f)	0 (f)
N _{H,nucleus} (10 ²² cm ⁻²)	0.08 ^{+0.02} _{-0.02}	0.08 (t)	0.08 (t)
N _{H,AGN} (10 ²⁴ cm ⁻²)	0.112 (f)	0.112 (t)	0.112 (t)
C-thin Fraction	0.194 (f)	0.194 (t)	0.194 (t)
N _{H,host} HMXB (10 ²² cm ⁻²)	7.92 (t)	...
kT ₁ (keV)	0.67 ^{+0.03} _{-0.03}	0.67 (t)	0.67 (t)	0.67 (t)	0.67 (t)
n _{e,1} (cm ⁻³)	0.00	4.1 × 10 ⁻²	1.5 × 10 ⁻²	4.0 × 10 ⁻³	9.7 × 10 ⁻⁴
kT ₂ (keV)	0.27 ^{+0.08} _{-0.27}	0.27 (t)	0.27 (t)	0.27 (t)	0.27 (t)
n _{e,2} (cm ⁻³)	0.00	0.00	0.00	2.7 × 10 ⁻³	9.2 × 10 ⁻⁴
E _{line,1} (keV)	0.879 ^{+0.024} _{-0.015}
EW _{line,1} (keV)	0.038 ^{+0.011} _{-0.013}
Line ID	Fe XVIII
E _{line,2} (keV)	1.003 ^{+0.019} _{-0.010}
EW _{line,2} (keV)	0.053 ^{+0.013} _{-0.013}
Line ID	Fe XXI
E _{line,3} (keV)	2.085 ^{+0.085} _{-0.090}	1.854 ^{+0.041} _{-0.050}
σ _{line3} (keV)	0.242 ^{+0.074} _{-0.063}	0 (f)
EW _{line,3} (keV)	0.133 ^{+0.045} _{-0.045}	0.368 ^{+0.358} _{-0.272}
Line ID	Si XIV	Si XIII
E _{line,4} (keV)	6.687 ^{+0.034} _{-0.045}	6.687 (t)	...
EW _{line,4} (keV)	0.121 ^{+0.040} _{-0.034}	1.431 ^{+2.211} _{-1.355}	...
Line ID	Fe XXV	Fe XXV	...
O/O _⊙ ^b	...	0.9 ^{+1.8} _{-0.7}	1.1 ^{+0.6} _{-0.4}	0.5 ^{+0.7} _{-0.2}	0.6 ^{+2.3} _{-0.3}
Mg/Mg _⊙ ^b	...	0.5 ^{+1.8} _{-0.5}	0.9 ^{+0.5} _{-0.4}	1.2 ^{+0.5} _{-0.4}	0.9 ^{+0.7} _{-0.5}
Si/Si _⊙ ^b	...	4.5 ^{+0.5} _{-2.2}	1.3 ^{+0.7} _{-0.6}	1.5 ^{+0.7} _{-0.6}	1 (f)
Fe/Fe _⊙ ^b	...	0.3 ^{+0.5} _{-0.2}	0.4 ^{+0.2} _{-0.1}	0.3 ^{+0.2} _{-0.1}	0.3 ^{+0.4} _{-0.1}
f _{0.5–2 keV} (10 ⁻¹⁴ erg s ⁻¹ cm ⁻²) ^c	5.26 ^{+0.10} _{-0.11}	0.56 ^{+0.03} _{-0.10}	1.38 ^{+0.04} _{-0.10}	2.03 ^{+0.07} _{-0.10}	2.09 ^{+0.10} _{-0.41}
f _{2–10 keV} (10 ⁻¹⁴ erg s ⁻¹ cm ⁻²) ^c	74.47 ^{+1.26} _{-1.20}	3.69 ^{+0.25} _{-0.25}	2.38 ^{+0.24} _{-0.23}	1.98 ^{+0.37} _{-0.41}	0.08 ^{+0.02} _{-0.02}
L _{MEKAL,1} (10 ⁴⁰ erg s ⁻¹) ^d	0.00	1.38	5.20	6.52	6.00
L _{MEKAL,2} (10 ⁴⁰ erg s ⁻¹) ^d	0.00	0.00	0.00	2.10	2.47
L _{HMXB} (10 ⁴⁰ erg s ⁻¹)	10.69	...
L _{AGN,0.5–2keV} (10 ⁴¹ erg s ⁻¹) ^d	9.92	0.50	0.32	0.00	0.00
L _{AGN,2–10keV} (10 ⁴¹ erg s ⁻¹) ^d	28.56	1.44	0.90	0.00	0.00

^aBest-fit model: $N_{\text{H, Galactic}} \times \{f_{\text{nuclear NuSTAR}} \times N_{\text{H, nucleus}} \times (\text{MYTorus}[N_{\text{H, AGN}}, PL_{\text{AGN}}] + f_{\text{C-thin}} \times PL_{\text{AGN}} + N_{\text{H, nuclear HMXB}} \times PL_{\text{nuclear HMXB}}^{\text{cutoff}}) + (N_{\text{H, host HMXB}} \times PL_{\text{host HMXB}}^{\text{cutoff}} + \text{line}[1-4] + \text{MEKAL}_1 + \text{MEKAL}_2)\}$, where $N_{\text{H, Galactic}} = 1.26 \times 10^{20} \text{ cm}^{-2}$, the Galactic column density in the direction of Mrk 231 (Dickey & Lockman 1990). $f_{\text{nuclear NuSTAR}}$ is the fraction (< 1) of the NuSTAR spectrum of Teng et al. (2014), minus the two MEKAL models of the nuclear diffuse emission, within the given aperture, $N_{\text{H, nucleus}}$ is an additional absorbing column in the line of sight toward the nucleus, not seen in the shallow *Chandra* spectrum of Teng et al. (2014), $N_{\text{H, AGN}}$ is the absorbing column of the AGN emission calculated as part of the MYTorus model and PL_{AGN} is the direct AGN emission within the MYTorus model that also includes the scattered fraction and Fe lines, $f_{\text{C-thin}}$ is the fraction (= 0.19) of the “leaked” direct AGN emission, $N_{\text{H, nuclear HMXB}} \times PL_{\text{nuclear HMXB}}^{\text{cutoff}}$ is the highly obscured emission from HMXBs in the nucleus, $N_{\text{H, host HMXB}} \times PL_{\text{host HMXB}}^{\text{cutoff}}$ is the emission from HMXBs outside of the nucleus (only detected in annulus #3), line[1–4] are Gaussian fits to the emission lines, and MEKAL₁ and MEKAL₂ are two MEKAL models of the emission from the hot diffuse gas (see text for more detail). This best-fit model has χ^2 of 468.7 for 426 degrees of freedom ($\chi^2_{\nu} = 1.10$). (t) indicates that the value of the parameter is tied to be the same in all regions. (f) indicates that the value of the parameter is held fixed.

^bAtomic abundance relative to Solar value. All other elemental abundances fixed at Solar.

^cObserved flux.

^dAbsorption corrected luminosity.

Table 2. b) Simultaneous Model Fit to the Annular Regions (shock models)

Model Parameter ^a	Annulus 1	Annulus 2	Annulus 3	Annulus 4
Radial Distance (kpc)	1.0–2.0	2.0–6.0	6.0–16.0	16.0–40.0
Hardness Ratio	-0.107 ± 0.028	-0.648 ± 0.025	-0.636 ± 0.020	$-1.000^{+0.024}_{-0.000}$
Ratio to Nuclear NuSTAR Model	$0.0408^{+0.0028}_{-0.0028}$	$0.0268^{+0.0025}_{-0.0025}$	0 (f)	0 (f)
$N_{\text{H,AGN}}$ (10^{24} cm ⁻²)	0.112 (f)	0.112 (t)
C-thin Fraction	0.194 (f)	0.194 (t)
$N_{\text{H,host HMXB}}$ (10^{22} cm ⁻²)	$7.55^{+5.02}_{-3.32}$...
kT (keV)	$0.67^{+0.03}_{-0.03}$	0.67 (t)	0.67 (t)	0.67 (t)
n_e (cm ⁻³)	3.6×10^{-2}	1.5×10^{-2}	4.3×10^{-3}	1.0×10^{-3}
O/O _⊙ ^b	$0.8^{+1.4}_{-0.7}$	$0.6^{+0.5}_{-0.3}$	$1.0^{+0.6}_{-0.4}$	$1.3^{+0.7}_{-0.6}$
Mg/Mg _⊙ ^b	1 (f)	$0.6^{+0.4}_{-0.3}$	$0.8^{+0.4}_{-0.3}$	$0.5^{+0.5}_{-0.4}$
Si/Si _⊙ ^b	$6.0^{+5.8}_{-2.9}$	$1.2^{+0.7}_{-0.5}$	$1.2^{+0.6}_{-0.5}$	$3.4^{+2.3}_{-1.8}$
Fe/Fe _⊙ ^b	$0.4^{+0.5}_{-0.2}$	$0.3^{+0.1}_{-0.1}$	$0.3^{+0.1}_{-0.1}$	$0.4^{+0.2}_{-0.1}$
τ_u (10^{12} s cm ⁻³) ^c	$4.1^{+11.2}_{-2.1}$	4.1 (t)	4.1 (t)	4.1 (t)
$f_{0.5-2 \text{ keV}}$ (10^{-14} erg s ⁻¹ cm ⁻²) ^d	$0.57^{+0.03}_{-0.09}$	$1.39^{+0.05}_{-0.08}$	$2.01^{+0.08}_{-0.10}$	$2.06^{+0.11}_{-0.21}$
$f_{2-10 \text{ keV}}$ (10^{-14} erg s ⁻¹ cm ⁻²) ^d	$3.70^{+0.26}_{-0.26}$	$2.39^{+0.23}_{-0.25}$	$2.04^{+0.34}_{-0.36}$	$0.10^{+0.10}_{-0.02}$
$L_{\text{shock}, 0.5-10\text{keV}}$ (10^{40} erg s ⁻¹) ^e	1.26	5.26	8.61	8.86
$L_{\text{host HMXB}}$ (10^{40} erg s ⁻¹) ^e	12.78	...
$L_{\text{AGN}, 0.5-2\text{keV}}$ (10^{40} erg s ⁻¹) ^e	5.41	3.42	0.00	0.00
$L_{\text{AGN}, 2-10\text{keV}}$ (10^{40} erg s ⁻¹) ^e	15.58	9.84	0.00	0.00

^aBest-fit model: $N_{\text{H, Galactic}} \times \{f_{\text{nuclear NuSTAR}} \times N_{\text{H, nucleus}} \times (\text{MYTorus}[N_{\text{H, AGN}}, PL_{\text{AGN}}] + f_{\text{C-thin}} \times PL_{\text{AGN}} + N_{\text{H, nuclear HMXB}} \times PL_{\text{nuclear HMXB}}^{\text{cutoff}}) + (N_{\text{H, host HMXB}} \times PL_{\text{host HMXB}}^{\text{cutoff}} + \text{vpshock})\}$, where $N_{\text{H, Galactic}} = 1.26 \times 10^{20}$ cm⁻², the Galactic column density in the direction of Mrk 231 (Dickey & Lockman 1990), $f_{\text{nuclear NuSTAR}}$ is the fraction (< 1) of the NuSTAR spectrum of Teng et al. (2014), minus the two MEKAL models of the nuclear diffuse emission, within the given aperture, $N_{\text{H, nucleus}}$ is an additional absorbing column in the line of sight toward the nucleus, not seen in the shallow *Chandra* spectrum of Teng et al. (2014), $N_{\text{H, AGN}}$ is the absorbing column of the AGN emission calculated as part of the MYTorus model and PL_{AGN} is the direct AGN emission within the MYTorus model that also includes the scattered fraction and Fe lines, $f_{\text{C-thin}}$ is the fraction (= 0.19) of the “leaked” direct AGN emission, $N_{\text{H, nuclear HMXB}} \times PL_{\text{nuclear HMXB}}^{\text{cutoff}}$ is the highly obscured emission from HMXBs in the nucleus, $N_{\text{H, host HMXB}} \times PL_{\text{host HMXB}}^{\text{cutoff}}$ is the emission from HMXBs outside of the nucleus (only detected in annulus #3), and vpshock is a constant temperature, plane-parallel shock plasma model of the emission from the hot diffuse gas (see text for more detail). This best-fit model has χ^2 of 227.4 for 236 degrees of freedom ($\chi^2_{\nu} = 0.96$). (t) indicates that the value of the parameter is tied to be the same in all regions. (f) indicates that the value of the parameter is held fixed.

^bAtomic abundance relative to Solar value. All other elemental abundances fixed at Solar.

^cUpper limit on the ionization time scale ($\tau = \int n_e dt$). The lower limit is fixed at 0.

^dObserved flux.

^eAbsorption corrected luminosity.

Table 3. a) Simultaneous Model Fit to the Neutral Outflow Regions (MEKAL models)

Model Parameter ^a	East	South	West	North
Position Angle(°)	45–135	135–225	225–315	–45–45
Radial Distance (kpc)	1.0–2.0	1.0–2.0	1.0–2.0	1.0–2.0
Hardness Ratio	-0.167 ± 0.048	-0.104 ± 0.061	0.034 ± 0.066	0.036 ± 0.055
Ratio to Nuclear NuSTAR Model	$0.0096^{+0.0007}_{-0.0007}$	0.0096 (t)	0.0096 (t)	0.0096 (t)
$N_{\text{H,AGN}}$ (10^{24} cm^{-2})	0.112 (f)	0.112 (t)	0.112 (t)	0.112 (t)
C-thin Fraction	0.194 (f)	0.194 (t)	0.194 (t)	0.194 (t)
kT (keV)	$0.75^{+0.13}_{-0.14}$	0.75 (t)	0.75 (t)	0.75 (t)
n_e (cm^{-3})	5.4×10^{-2}	3.6×10^{-2}	2.8×10^{-2}	4.7×10^{-2}
$\text{O}/\text{O}_{\odot}$ ^b	1 (f)	1 (f)	1 (f)	1 (f)
$\text{Mg}/\text{Mg}_{\odot}$ ^b	1 (f)	1 (f)	1 (f)	1 (f)
$\text{Si}/\text{Si}_{\odot}$ ^b	$4.0^{+3.7}_{-2.4}$	1 (f)	1 (f)	1 (f)
$\text{Fe}/\text{Fe}_{\odot}$ ^b	$0.3^{+0.3}_{-0.2}$	0.3 (f)	0.3 (f)	$0.1^{+0.4}_{-0.1}$
$f_{0.5-2 \text{ keV}}$ ($10^{-15} \text{ erg s}^{-1} \text{ cm}^{-2}$) ^c	$2.02^{+0.18}_{-0.27}$	$1.19^{+0.13}_{-0.16}$	$0.97^{+0.14}_{-0.15}$	$1.43^{+0.19}_{-0.26}$
$f_{2-10 \text{ keV}}$ ($10^{-15} \text{ erg s}^{-1} \text{ cm}^{-2}$) ^c	$8.78^{+0.65}_{-0.65}$	$8.70^{+0.55}_{-0.64}$	$8.68^{+0.54}_{-0.65}$	$8.73^{+0.56}_{-0.63}$
L_{MEKAL} ($10^{39} \text{ erg s}^{-1}$) ^d	6.51	2.57	1.54	3.79
$L_{\text{AGN},0.5-2\text{keV}}$ ($10^{40} \text{ erg s}^{-1}$) ^d	1.28	1.28	1.28	1.28
$L_{\text{AGN},2-10\text{keV}}$ ($10^{40} \text{ erg s}^{-1}$) ^d	3.68	3.68	3.68	3.68

^aBest-fit model: $N_{\text{H, Galactic}} \times \{f_{\text{nuclear NuSTAR}} \times N_{\text{H, nucleus}} \times (\text{MYTorus}[N_{\text{H, AGN}}, PL_{\text{AGN}}] + f_{\text{C-thin}} \times PL_{\text{AGN}} + N_{\text{H, nuclear HMXB}} \times PL_{\text{nuclear HMXB}}^{\text{cutoff}}) + \text{MEKAL}_1\}$, where $N_{\text{H, Galactic}} = 1.26 \times 10^{20} \text{ cm}^{-2}$, the Galactic column density in the direction of Mrk 231 (Dickey & Lockman 1990), $f_{\text{nuclear NuSTAR}}$ is the fraction (< 1) of the NuSTAR spectrum of Teng et al. (2014), minus the two MEKAL models of the nuclear diffuse emission, within the given aperture, $N_{\text{H, nucleus}}$ is an additional absorbing column in the line of sight toward the nucleus, not seen in the shallow *Chandra* spectrum of Teng et al. (2014), $N_{\text{H, AGN}}$ is the absorbing column of the AGN emission calculated as part of the MYTorus model and PL_{AGN} is the direct AGN emission within the MYTorus model that also includes the scattered fraction and Fe lines, $f_{\text{C-thin}}$ is the fraction ($= 0.19$) of the “leaked” direct AGN emission, $N_{\text{H, nuclear HMXB}} \times PL_{\text{nuclear HMXB}}^{\text{cutoff}}$ is the highly obscured emission from HMXBs in the nucleus, and MEKAL_1 is a MEKAL model of the emission from the hot diffuse gas (see text for more detail). This best-fit model has χ^2 of 87.2 for 72 degrees of freedom ($\chi^2_{\nu} = 1.21$). (t) indicates that the value of the parameter is tied to be the same in all regions. (f) indicates that the value of the parameter is held fixed.

^bAtomic abundance relative to Solar value. All other elemental abundances fixed at Solar.

^cObserved flux.

^dAbsorption corrected luminosity.

Table 3. b) Simultaneous Model Fit to the Neutral Outflow Regions (shock models)

Model Parameter ^a	East	South	West	North
Position Angle(°)	45–135	135–225	225–315	–45–45
Radial Distance (kpc)	1.0–2.0	1.0–2.0	1.0–2.0	1.0–2.0
Hardness Ratio	–0.167 ± 0.048	–0.104 ± 0.061	0.034 ± 0.066	0.036 ± 0.055
Ratio to Nuclear NuSTAR Model	0.0097 ^{+0.0007} _{–0.0007}	0.0097 (t)	0.0097 (t)	0.0097 (t)
$N_{\text{H,AGN}}$ (10^{24} cm ^{–2})	0.112 (f)	0.112 (t)	0.112 (t)	0.112 (t)
C-thin Fraction	0.194 (f)	0.194 (t)	0.194 (t)	0.194 (t)
kT (keV)	0.70 ^{+0.17} _{–0.14}	0.70 (t)	0.70 (t)	0.70 (t)
n_e (cm ^{–3})	5.7×10^{-2}	3.2×10^{-2}	2.8×10^{-2}	4.5×10^{-2}
O/O _⊙ ^b	0.8 ^{+2.8} _{–0.8}	1 (f)	1 (f)	1 (f)
Mg/Mg _⊙ ^b	1 (f)	1 (f)	1 (f)	1 (f)
Si/Si _⊙ ^b	3.9 ^{+4.0} _{–2.2}	1 (f)	1 (f)	4.3 ^{+8.2} _{–3.6}
Fe/Fe _⊙ ^b	0.2 ^{+0.4} _{–0.1}	0.4 ^{+3.9} _{–0.3}	0.3 (f)	0.1 ^{+0.6} _{–0.1}
τ_u (10^{12} s cm ^{–3}) ^c	> 2.8	> 2.8 (t)	> 2.8 (t)	> 2.8 (t)
$f_{0.5-2}$ keV (10^{-15} erg s ^{–1} cm ^{–2}) ^d	2.00 ^{+0.16} _{–0.38}	1.17 ^{+0.12} _{–0.37}	0.98 ^{+0.14} _{–0.14}	1.46 ^{+0.17} _{–0.33}
f_{2-10} keV (10^{-15} erg s ^{–1} cm ^{–2}) ^d	8.80 ^{+0.61} _{–0.62}	8.73 ^{+0.62} _{–0.62}	8.72 ^{+0.63} _{–0.62}	8.77 ^{+0.62} _{–0.62}
$L_{\text{shock},0.5-10\text{keV}}$ (10^{39} erg s ^{–1}) ^e	6.29	2.40	1.53	3.82
$L_{\text{AGN},0.5-2\text{keV}}$ (10^{40} erg s ^{–1}) ^e	1.28	1.28	1.28	1.28
$L_{\text{AGN},2-10\text{keV}}$ (10^{40} erg s ^{–1}) ^e	3.70	3.70	3.70	3.70

^aBest-fit model: $N_{\text{H, Galactic}} \times \{f_{\text{nuclear NuSTAR}} \times N_{\text{H, nucleus}} \times (\text{MYTorus}[N_{\text{H, AGN}}, PL_{\text{AGN}}] + f_{\text{C-thin}} \times PL_{\text{AGN}} + N_{\text{H, nuclear HMXB}} \times PL_{\text{nuclear HMXB}}^{\text{cutoff}}) + \text{vpshock}\}$, where $N_{\text{H, Galactic}} = 1.26 \times 10^{20}$ cm^{–2}, the Galactic column density in the direction of Mrk 231 (Dickey & Lockman 1990), $f_{\text{nuclear NuSTAR}}$ is the fraction (< 1) of the NuSTAR spectrum of Teng et al. (2014), minus the two MEKAL models of the nuclear diffuse emission, within the given aperture, $N_{\text{H, nucleus}}$ is an additional absorbing column in the line of sight toward the nucleus, not seen in the shallow *Chandra* spectrum of Teng et al. (2014), $N_{\text{H, AGN}}$ is the absorbing column of the AGN emission calculated as part of the MYTorus model and PL_{AGN} is the direct AGN emission within the MYTorus model that also includes the scattered fraction and Fe lines, $f_{\text{C-thin}}$ is the fraction (= 0.19) of the “leaked” direct AGN emission, $N_{\text{H, nuclear HMXB}} \times PL_{\text{nuclear HMXB}}^{\text{cutoff}}$ is the highly obscured emission from HMXBs in the nucleus, and vpshock is a constant temperature, plane-parallel shock plasma model of the emission from the hot diffuse gas (see text for more detail). This best-fit model has χ^2 of 86.3 for 68 degrees of freedom ($\chi^2_{\nu}=1.27$). (t) indicates that the value of the parameter is tied to be the same in all regions. (f) indicates that the value of the parameter is held fixed.

^bAtomic abundance relative to Solar value. All other elemental abundances fixed at Solar.

^cUpper limit on the ionization time scale ($\tau = \int n_e dt$). The lower limit is fixed at 0.

^dObserved flux.

^eAbsorption corrected luminosity.

Table 4. Simultaneous Model Fit to the Tidal Arc Regions

Model Parameter ^a	Arc	East	West	North
Position Angle(°)	125-215	35-125	215-305	-55-35
Radial Distance (kpc)	2.0-4.5	2.0-4.5	2.0-4.5	2.0-4.5
Hardness Ratio	$-0.708^{+0.065}_{-0.061}$	-0.613 ± 0.062	$-0.514^{+0.080}_{-0.074}$	$-0.710^{+0.064}_{-0.060}$
Ratio to Nuclear NuSTAR Model	$0.0049^{+0.0006}_{-0.0006}$	0.0049 (t)	0.0049 (t)	0.0049 (t)
$N_{\text{H,AGN}}$ (10^{24} cm ⁻²)	0.112 (f)	0.112 (t)	0.112 (t)	0.112 (t)
C-thin Fraction	0.194 (f)	0.194 (t)	0.194 (t)	0.194 (t)
kT (keV)	$0.65^{+0.06}_{-0.07}$	0.65 (t)	0.65 (t)	0.65 (t)
n_e (cm ⁻³)	1.6×10^{-2}	2.2×10^{-2}	1.5×10^{-2}	2.3×10^{-2}
O/O _⊙ ^b	$2.4^{+31.4}_{-1.7}$	$0.6^{+1.4}_{-0.5}$	$1.2^{+6.9}_{-1.2}$	$0.3^{+1.1}_{-0.3}$
Mg/Mg _⊙ ^b	$1.0^{+17.4}_{-1.0}$	$0.7^{+1.3}_{-0.7}$	$0.9^{+6.2}_{-0.9}$	$1.2^{+1.7}_{-0.9}$
Si/Si _⊙ ^b	$3.7^{+33.5}_{-2.7}$	$0.9^{+1.6}_{-0.9}$	$1.6^{+7.9}_{-1.6}$	$0.3^{+1.3}_{-0.3}$
Fe/Fe _⊙ ^b	$0.6^{+8.3}_{-0.4}$	$0.2^{+0.3}_{-0.1}$	$0.3^{+1.7}_{-0.2}$	$0.3^{+0.4}_{-0.2}$
E _{line,1} (keV)	$1.242^{+0.028}_{-0.045}$
EW _{line,1} (keV)	$0.163^{+0.179}_{-0.101}$
Line ID	Ne X or Fe XIX
E _{line,2} (keV)	$1.670^{+0.157}_{-0.060}$
EW _{line,2} (keV)	$0.281^{+0.245}_{-0.221}$
Line ID	Si XIII
$f_{0.5-2}$ keV (10^{-15} erg s ⁻¹ cm ⁻²) ^c	$2.92^{+0.21}_{-1.05}$	$2.51^{+0.17}_{-0.56}$	$1.53^{+0.13}_{-0.57}$	$2.86^{+0.21}_{-0.63}$
f_{2-10} keV (10^{-15} erg s ⁻¹ cm ⁻²) ^c	$4.46^{+0.47}_{-0.48}$	$4.48^{+0.50}_{-0.49}$	$4.42^{+0.50}_{-0.43}$	$4.49^{+0.50}_{-0.51}$
LMEKAL (10^{40} erg s ⁻¹) ^d	1.06	1.02	0.56	1.17
L _{AGN,0.5-2keV} (10^{40} erg s ⁻¹) ^d	0.64	0.64	0.64	0.64
L _{AGN,2-10keV} (10^{40} erg s ⁻¹) ^d	1.85	1.85	1.85	1.85

^aBest-fit model: $N_{\text{H, Galactic}} \times \{f_{\text{nuclear NuSTAR}} \times N_{\text{H, nucleus}} \times (\text{MYTorus}[N_{\text{H, AGN}}, PL_{\text{AGN}}] + f_{\text{C-thin}} \times PL_{\text{AGN}} + N_{\text{H, nuclear HMXB}} \times PL_{\text{nuclear HMXB}}^{\text{cutoff}} + \text{line}[1-2] + \text{MEKAL}_1)\}$, where $N_{\text{H, Galactic}} = 1.26 \times 10^{20}$ cm⁻², the Galactic column density in the direction of Mrk 231 (Dickey & Lockman 1990), $f_{\text{nuclear NuSTAR}}$ is the fraction (< 1) of the NuSTAR spectrum of Teng et al. (2014), minus the two MEKAL models of the nuclear diffuse emission, within the given aperture, $N_{\text{H, nucleus}}$ is an additional absorbing column in the line of sight toward the nucleus, not seen in the shallow *Chandra* spectrum of Teng et al. (2014), $N_{\text{H, AGN}}$ is the absorbing column of the AGN emission calculated as part of the MYTorus model and PL_{AGN} is the direct AGN emission within the MYTorus model that also includes the scattered fraction and Fe lines, $f_{\text{C-thin}}$ is the fraction (= 0.19) of the “leaked” direct AGN emission, $N_{\text{H, nuclear HMXB}} \times PL_{\text{nuclear HMXB}}^{\text{cutoff}}$ is the highly obscured emission from HMXBs in the nucleus, line[1 - 2] are Gaussian fits to the emission lines, and MEKAL₁ is a MEKAL model of the emission from the hot diffuse gas (see text for more detail). This best-fit model has χ^2 of 49.1 for 67 degrees of freedom ($\chi^2_{\nu}=0.73$). (t) indicates that the value of the parameter is tied to be the same in all regions. (f) indicates that the value of the parameter is held fixed.

^bAtomic abundance relative to Solar value. All other elemental abundances fixed at Solar.

^cObserved flux.

^dAbsorption corrected luminosity.

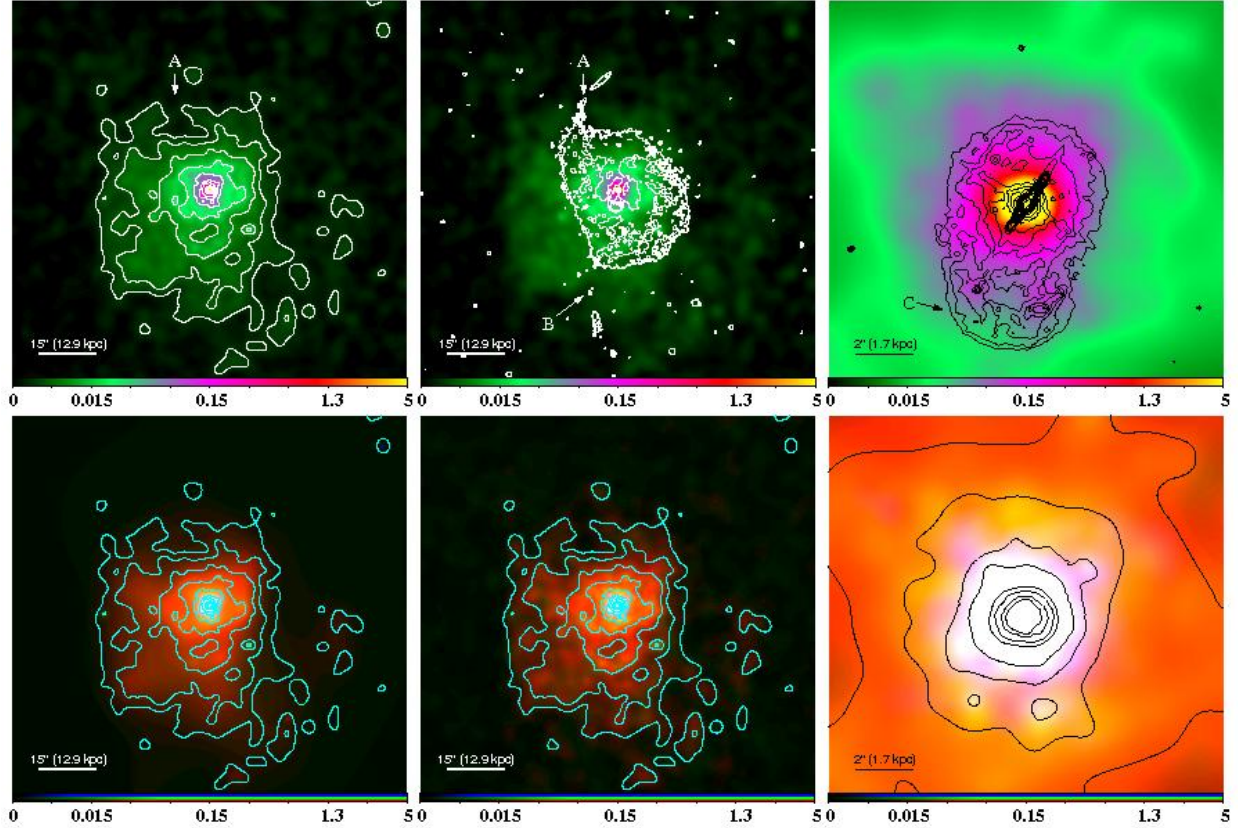


Fig. 1.— (*Top*) Adaptively smoothed full X-ray band (0.5 - 8 keV) merged images from all observations (0.52 Msec in total), on a logarithmic scale. North is up and East is to the left. The overlaid contours are (*left*) the full 0.5 - 8 keV contours at 2, 3, 5, 10, 25, 50, 100, 500, 1000, and 5000 σ , (*middle*) the contours of the optical *HST* image from RV11, and (*right*) the contours of the *HST* optical image zoomed-in to show the tidal star-forming arc ~ 3.5 kpc south of the nucleus. The cross-like pattern in the center of the optical image in both the middle and right panels is an artifact of the strong central PSF. Labels A, B, and C point to the northern tidal tail, the southern tidal tail, and the southern tidal arc, respectively. (*Bottom*) False-color X-ray images of adaptively smoothed images overlaid with the full X-ray band contours from the upper left panel. In all three of these bottom panels, red represents the 0.5 - 1 keV emission, green is 1 - 2 keV, and blue is 2 - 8 keV. The bottom left panel is smoothed using *csmooth* to emphasize the large-scale structure. The middle panel is smoothed using the *imageadapt* script designed to better show the small-scale structures. The bottom right panel is a zoomed-in version of the middle panel.

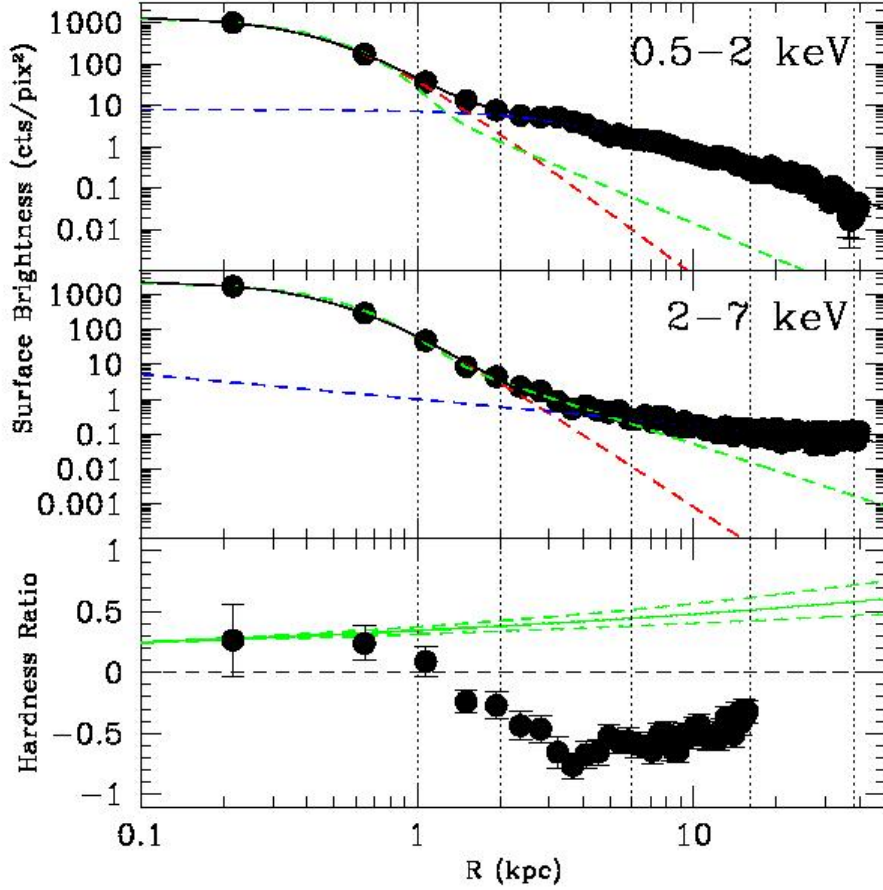


Fig. 2.— Radial profiles of Mrk 231 in the 0.5–2 keV and 2–7 keV bands. In the top two panels, the background-subtracted data points are represented by filled circles. A two-component β model is fitted to each profile (see text and Table 1) with the best fit shown as a black curve. The red and blue dash lines represent the inner and outer components of each model, respectively. The green dash lines in the top two panels represent the simulated PSF fit using two-component β models. The soft emission is extended beyond ~ 1 kpc and the hard emission is extended beyond ~ 6 kpc. The bottom panel is a radial profile of the hardness ratio, emphasizing the softness of the extended emission. The green curve shows the hardness ratio of the simulated PSF for comparison. The vertical dotted lines show the division between the annuli extraction regions for Tables 2a. and 2b. The drop in the hardness ratio from ~ 1 kpc to ~ 6 kpc reflects the increasing importance of the extended soft X-ray component relative to that of the central quasar. Beyond 16 kpc, the hardness ratio profile is not shown because it is unreliable – there are very few counts in the hard X-ray band on this scale and the soft X-ray emission is also very patchy.

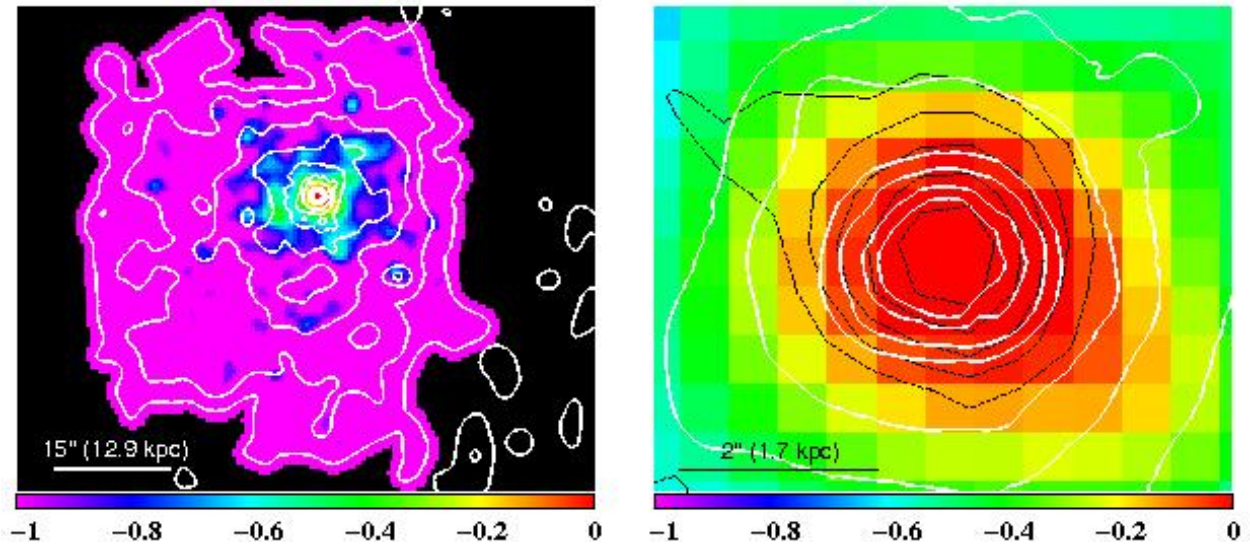


Fig. 3.— Pixel-to-pixel hardness ratio map of Mrk 231. North is up and East is to the left. In both panels, the image is smoothed with a 4-pixel Gaussian and the *Chandra* 0.5–8 keV contours are shown in white for comparison. The left panel shows the extended soft emission and the right panel zooms in on the nuclear region. In the right panel, the contours of the PSF hardness ratio (Figure 2) are shown as dashed black lines for comparison. Note that since the PSF has a different hardness ratio than the data, this is only a comparison of the morphology of the hardness ratio, not its absolute value. The faint northeast tail in the PSF contours is an artifact of the simulated PSF. Note the slight asymmetry of the nuclear hardness ratio map (color map in the right panel) extending to the west.

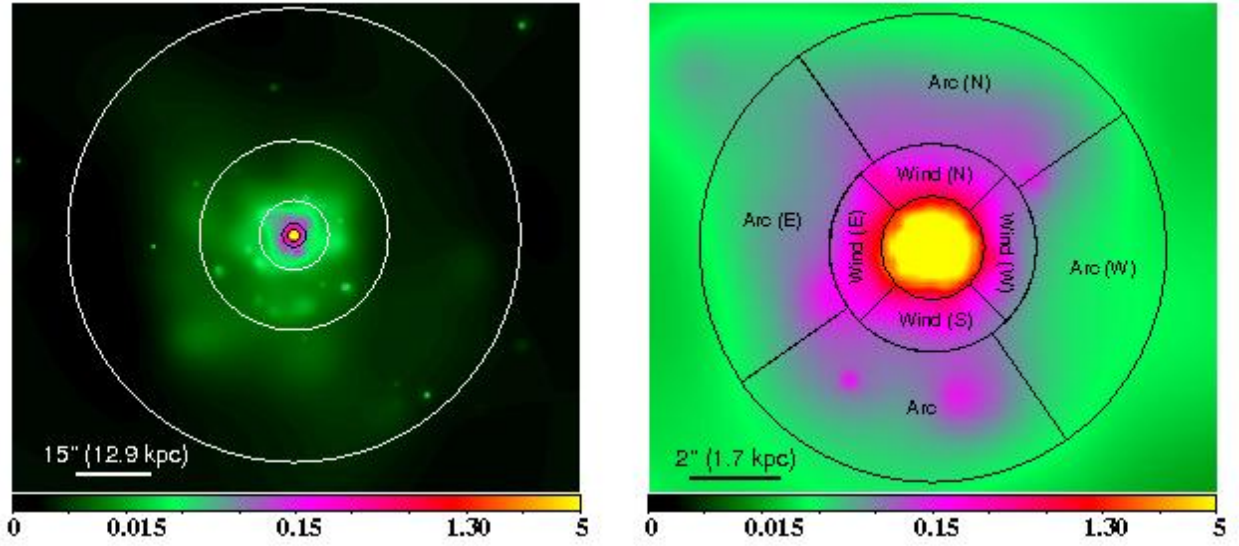


Fig. 4.— Full X-ray band image showing the different extraction regions used for the spectral analysis in §3.2. North is up and East is to the left. (*Left*) Annular regions. The nucleus and annuli #1-4 have outer radii $R = 1.0$ kpc, 2.0 kpc, 6 kpc, 16 kpc, and 40 kpc, respectively. (*Right*) The outflow and tidal arc extraction regions. The outflow extraction regions corresponds to annulus #1 (1 – 2 kpc) divided into four equal-size quadrants covering PA = $-45 - +45^\circ$ (N), $+45 - +135^\circ$ (E), $+135 - +225^\circ$ (S), and $+225 - +315^\circ$ (W). The tidal arc region extends over $R = 2.0 - 4.5$ kpc and PA = $+125 - +215^\circ$ (Arc). The comparison regions span PA = $+35 - +125^\circ$ (E), $+215 - +305^\circ$ (W), $-55 - +35^\circ$ (N).

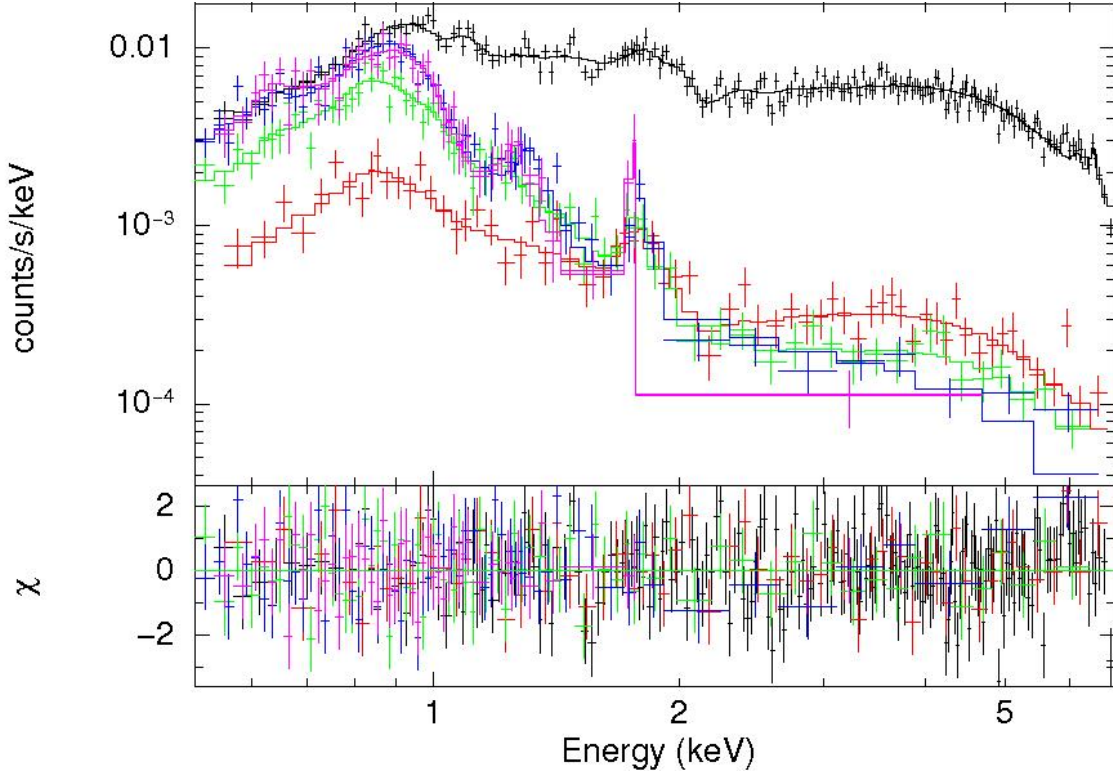


Fig. 5.— (*Top*) Spectra extracted from the annular regions shown with the best-fit model to the simultaneous fit. (*Bottom*) Residuals (data minus model) where error bars of size one correspond to one sigma. The colors represent the nucleus binned to 8σ above the background (black), annulus #1 binned to 8σ above the background (red), annulus #2 binned to 4σ above the background (green), annulus #3 binned to 4σ above the background (blue), and annulus #4 binned to 3σ above the background (magenta). Note the presence of Mg XI 1.352 keV and Si XIII 1.864 keV in many of these spectra. The model to annulus #3 is underestimated near 6 keV. This may indicate the presence of Fe XXV 6.7 keV outside of the nucleus (see Figure 11 for a more detailed fitting of the spectrum). The parameters of the best fits are listed in Table 2a.

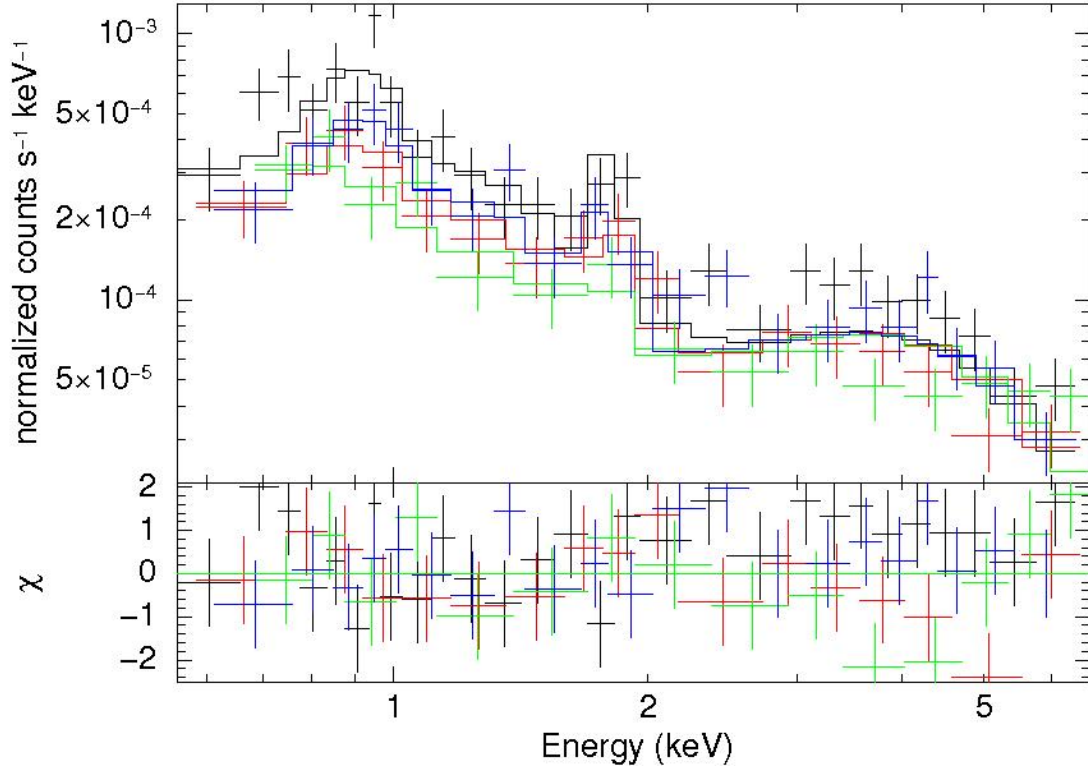


Fig. 6.— (*Top*) Spectra extracted from the outflow regions shown with the best-fit model to the simultaneous fit. (*Bottom*) Residuals (data minus model) where error bars of size one correspond to one sigma. Here, black is east, red is south, green is west, blue is north. The spectra are binned to at least 15 counts per bin. The best-fit parameters are listed in Table 3a. Si XIII 1.864 keV is detected in the eastern and northern regions.

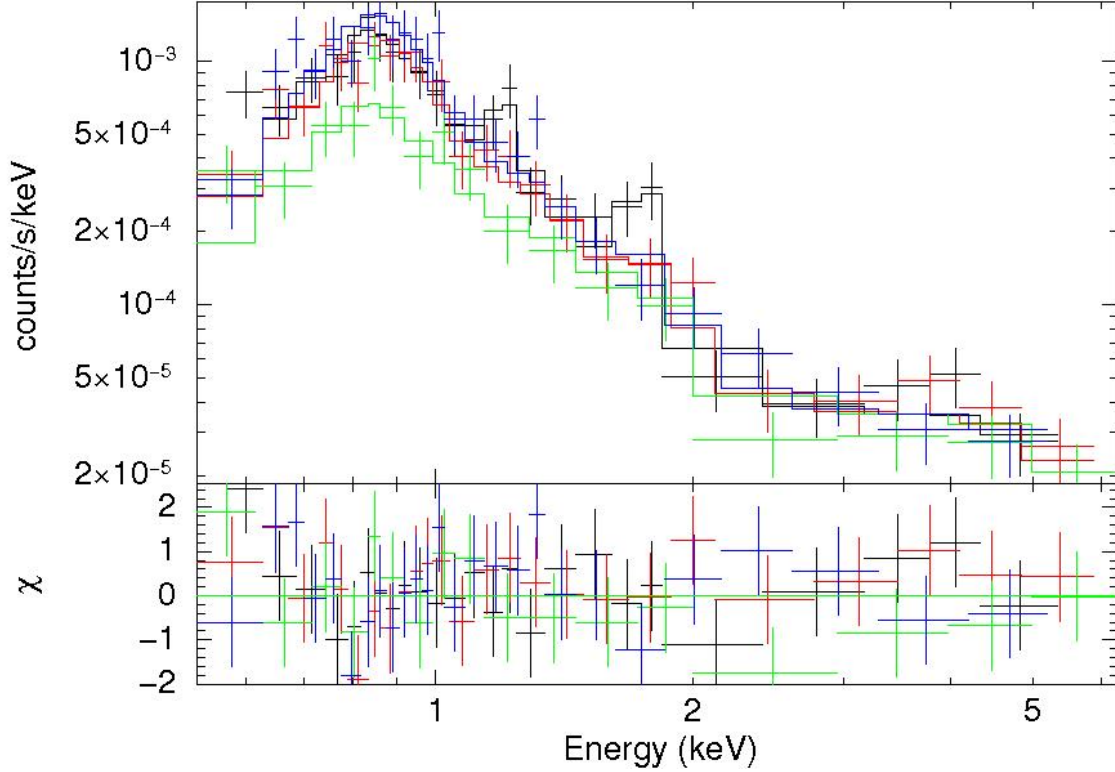


Fig. 7.— (*Top*) Spectra extracted from the tidal arc regions shown with the best-fit model to the simultaneous fit. (*Bottom*) Residuals (data minus model) where error bars of size one correspond to one sigma. The spectra are binned to at least 15 counts per bin. The black spectrum is the bright arc itself (PA: $125 - 215^\circ$). The red is the eastern comparison region (PA: $35 - 125^\circ$), the green is the western comparison region ($215 - 305^\circ$), and the blue is the northern comparison region (PA: $-55 - 35^\circ$). The parameters of the best fits are listed in Table 4. Note the detection of the Mg XI 1.352 keV and Si XIII 1.864 keV emission lines in the tidal arc spectrum, indicating the presence of α -element enhancement due to the starburst in this region.

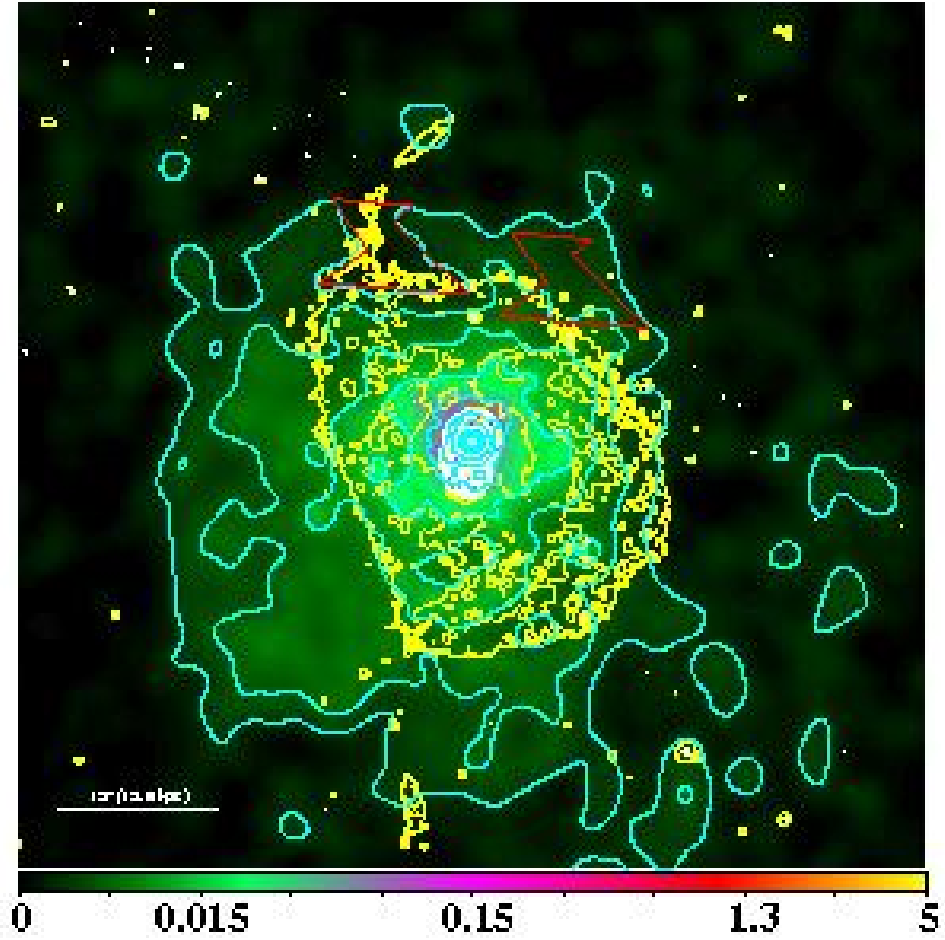


Fig. 8.— The polygonal extraction regions (in red) used to derive the X-ray spectra of the northern tidal tail (on the left) and a comparison region (on the right), shown against the contours of the full X-ray band image (cyan) and the *HST* optical image on large scale (yellow) and small scale (white). North is up and East is to the left.

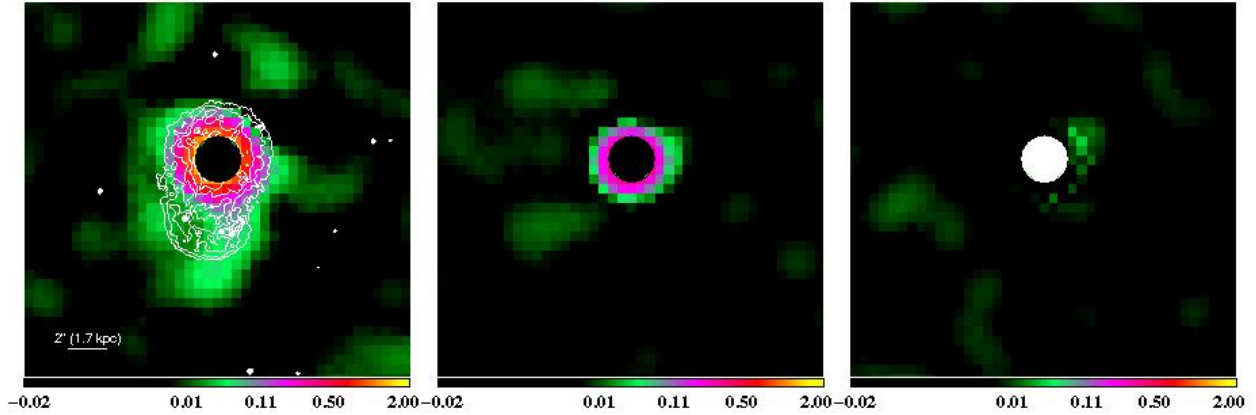


Fig. 9.— Continuum-subtracted maps of the line emission in Mrk 231. North is up and East is to the left. (*left*) Si XIII (1.70–1.95 keV) compared with the *HST* optical image (contours), (*middle*) Fe K α (6.31–6.56 keV), and (*right*) Fe XXV + Fe XXVI (6.56–6.90 keV). The emission is smoothed with a 4-pixel Gaussian. The bright continuum emission from the central quasar makes the maps unreliable within the central 3.0 kpc diameter region; this region is masked in the three panels. Filamentary Si XIII emission is seen out to ~ 5 kpc. Extended Fe XXV + Fe XXVI emission may also be present ~ 3 kpc north-west of the nucleus.

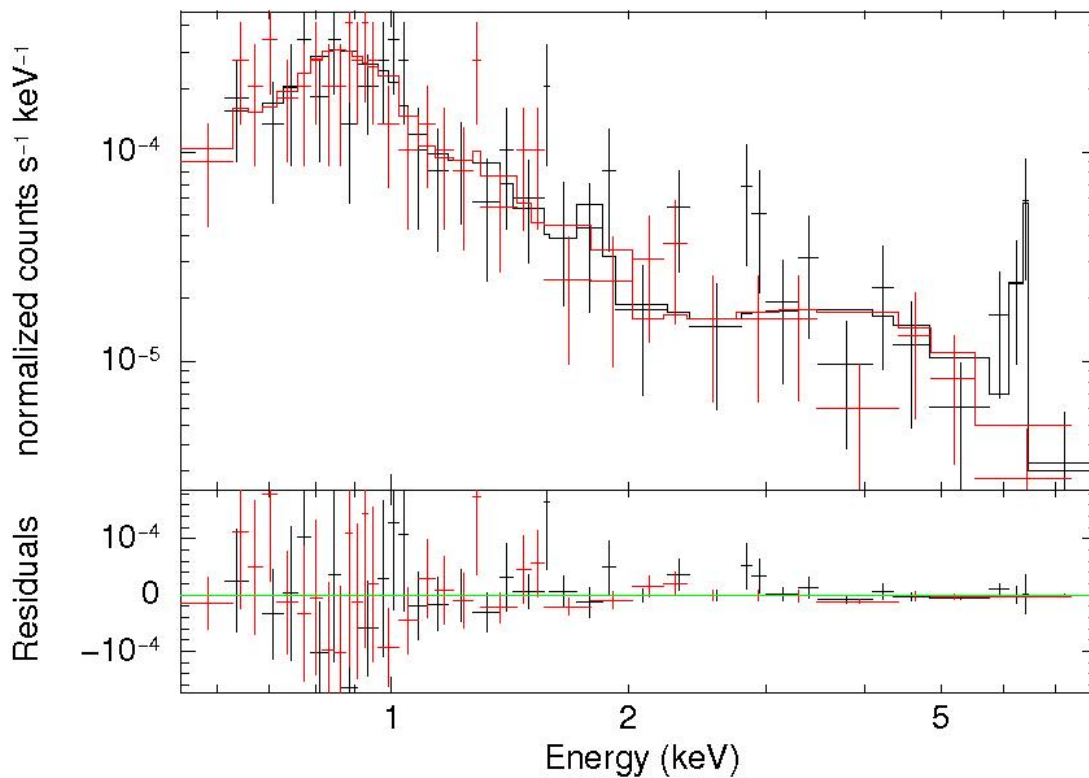


Fig. 10.— (*Top*) Spectrum (black data points) extracted from a 2-arcsec diameter region centered on the brightest part of the Fe XXV 6.7 keV + Fe XXVI 6.9 keV extension northwest of the nucleus in Figure 9. (*Bottom*) Residuals (data minus model). The spectrum in red is from an equal-size region on the opposite side of the nucleus where there is no obvious Fe XXV + Fe XXVI emission in the line emission map. The displayed spectra are binned to at least 3 counts per bin, while the model was fit to unbinned data using Cash statistics. There is a tentative detection of Fe XXV 6.7 keV outside of the nucleus (see §3.2.5).

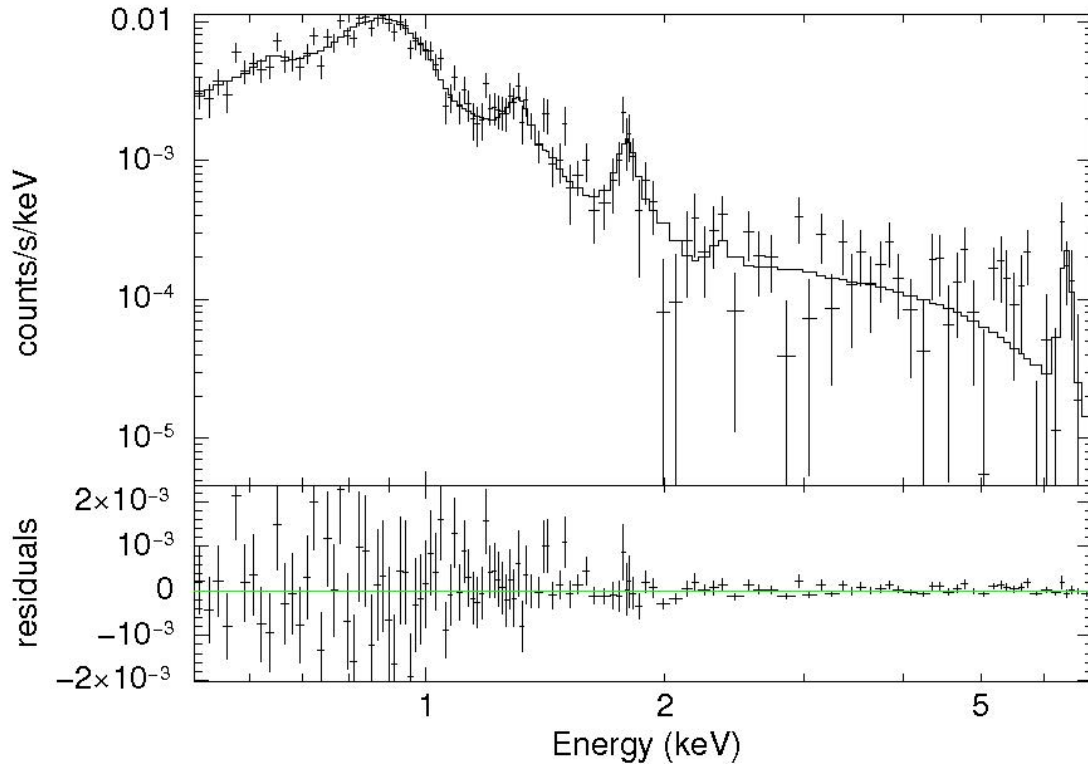


Fig. 11.— (*Top*) Spectrum of annulus #3 with a finer binning than Figure 5 (at least 15 counts per bin). (*Bottom*) Residuals (data minus model) where error bars of size one correspond to one sigma. The best-fit model shown in Figure 5 is applied with the addition of a narrow line at 6.7 keV to simulate Fe XXV emission.